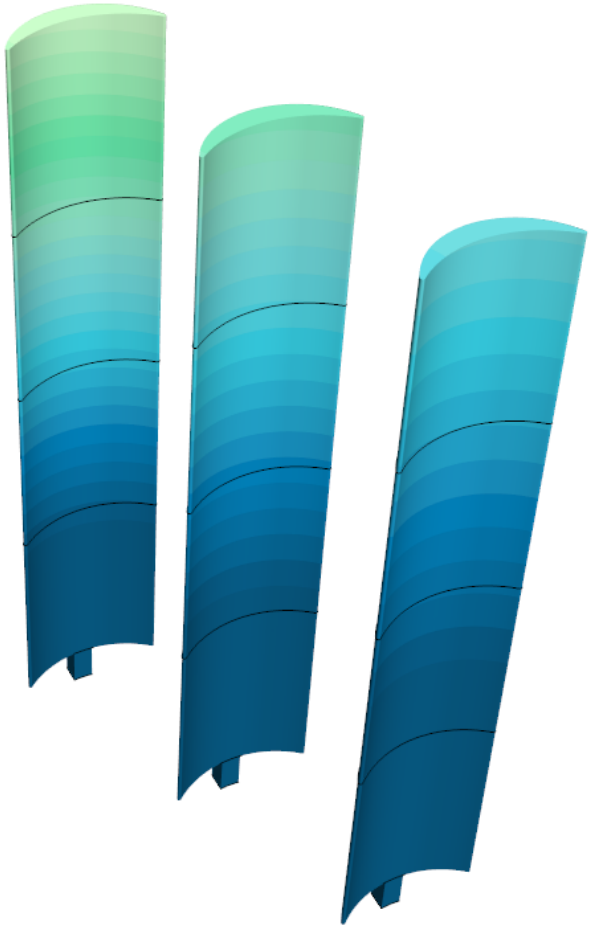

Fluid-Structure Interaction Analysis of Multiple Wingsails

Master's thesis in Mobility Engineering

GLÓDÍS HERMANNSDÓTTIR
CLARA TOUS BOSCH

DEPARTMENT OF MECHANICS AND MARITIME SCIENCES
CHALMERS UNIVERSITY OF TECHNOLOGY
Gothenburg, Sweden 2025
www.chalmers.se

Master's thesis 2025

Fluid-Structure Interaction Analysis of Multiple Wingsails

GLÓDÍS HERMANNSDÓTTIR
CLARA TOUS BOSCH

CHALMERS
UNIVERSITY OF TECHNOLOGY

Department of Mechanics and Maritime Sciences
Division of Marine Technology
Chalmers University of Technology
Gothenburg, Sweden 2025

Fluid-Structure Interaction Analysis of Multiple Wingsails
GLÓDÍS HERMANNSDÓTTIR
CLARA TOUS BOSCH

Supervisor: Heng Zhu, Department of Mechanics and Maritime Sciences
Examiner: Huadong Yao, Department of Mechanics and Maritime Sciences

Master's Thesis 2025
Department of Mechanics and Maritime Sciences
Division of Marine Technology
Chalmers University of Technology
SE-412 96 Gothenburg
Telephone +46 31 772 1000

Cover: FSI simulation showing the displacement of three crescent-shaped wingsails.

Typeset in LaTeX
Printed by Chalmers Reproservice
Gothenburg, Sweden 2025

Fluid-Structure Interaction Analysis of Multiple Wingsails
GLÓDÍS HERMANNSDÓTTIR
CLARA TOUS BOSCH
Department of Mechanics and Maritime Sciences
Chalmers University of Technology

Abstract

The maritime sector contributes around 3% of CO_2 emissions. The International Maritime Organization (IMO) has a net-zero emission goal for the maritime sector by 2050. This goal has forced the industry to develop more environmentally friendly propulsion solutions, while wind-assisted ship propulsion is an alternative solution for sustainable shipping.

This thesis investigates the aerodynamic performance and fluid-structure interaction (FSI) among multiple wingsails with crescent-shaped profiles. A two-way coupled FSI simulation framework was developed by using computational fluid dynamics (CFD) integrated with finite element analysis (FEA). The CFD simulations were performed using improved delayed detached eddy simulation (IDDES). The FEA was based on a simplified structural model, where the wingsails are regarded as solid bodies, and the tip displacement due to global bending was focused. The arbitrary Lagrangian-Eulerian (ALE) approach was implemented with mesh morphing based on radial basis function (RBF).

FSI and CFD simulations are performed for three apparent wind angles (AWA): 60, 90, and 120 degrees. Results revealed that the wingsail closest to the bow of the ship experiences higher aerodynamic forces and stronger flutter than the other sails closer to the stern, indicating more critical flow. It was also found that the FSI has considerable negative effects on the thrust generation. This study is expected to provide guidance on wingsail structural design and multiple wingsail arrangements.

Keywords: fluid-structure interaction, wingsails, computational fluid dynamics, cambered profile, wind-assisted ship propulsion

Acknowledgements

I would like to thank everyone who contributed to this master's thesis at Chalmers University of Technology. First, I wish to express my sincere gratitude to my thesis partner, Glódís Hermannsdóttir, for her patience and dedication and for the positive energy she brought to our work together. This thesis has been both enjoyable and educational thanks to our amazing teamwork.

I would also like to express my appreciation to our supervisor, Heng Zhu, for his expert guidance, constructive feedback, and continuous support throughout this project. Your advice has helped make this work a smoother and more rewarding experience.

My thanks also go to our examiner, Huadong Yao, for his valuable input and thoughtful discussions during the evaluation process.

Finally, I am deeply grateful to my family and friends for their patience, support, and encouragement throughout this journey, especially to my parents, Tica and Josep, and my sisters, Berta and Cristina.

Clara Tous Bosch, Gothenburg, June 2025

I would like to express my sincere gratitude to everyone who contributed to this master's thesis at Chalmers University of Technology.

First, I would like to thank my thesis partner, Clara, for being such a reliable and supportive teammate throughout this project. Her dedication and valuable input made working on this thesis both smooth and enjoyable.

I am also deeply grateful to our supervisor, Heng Zhu, for his valuable guidance, constructive feedback, and consistent support throughout the project. His expertise greatly helped us navigate challenges and stay focused on our goals.

I would also like to thank our examiner, Huadong Yao, for his guidance and support throughout the thesis process. His involvement was greatly appreciated and contributed meaningfully to our work.

Finally, I am especially thankful to my family for their continued support, encouragement, and understanding throughout my academic journey.

Glódís Hermannsdóttir, Gothenburg, June 2025

List of Acronyms

Below is the list of acronyms that have been used throughout this thesis listed in alphabetical order:

AOA	Angle of Attack
ALE	Arbitrary Lagrangian-Eulerian
AWA	Apparent Wind Angle
BC	Boundary Condition
BL	Boundary Layer
CFD	Computational Fluid Dynamics
DES	Detached Eddy Simulation
FEA	Finite Element Analysis
FIV	Flow-Induced Vibrations
FSI	Fluid-Structure Interaction
FVM	Finite Volume Method
GHG	Greenhouse Gas
IDDES	Improved Delayed Detached Eddy Simulation
IMO	International Maritime Organization
LFMI	Laboratory of Fluid Mechanics and Instabilities
LSQ	Least Squares
NACA	(The United States) National Advisory Committee for Aeronautics
RANS	Reynolds-Averaged Navier–Stokes
RBF	Radial Basis Function
SIMPLE	Semi-implicit method for pressure-linked equations
SST	Shear Stress Transport
UNCTAD	United Nations Conference on Trade and Development Agency
URANS	Unsteady Reynolds-Averaged Navier–Stokes
VIV	Vortex-Induced Vibration
WASP	Wind Assisted Ship Propulsion
WT	Wind Tunnel

Nomenclature

Below is the nomenclature of variables that have been used throughout this thesis.

Variables

C_D	Drag Coefficient
C_L	Lift Coefficient
C_M	Moment Coefficient
E	Young Modulus
F_D	Drag Force
F_L	Lift Force
F_S	Side Force
F_T	Thrust Force
I	Moment of Inertia
L	Member Length
L_C	Chord Length
V_{AW}	Apparent Wind Angle
V_S	Ship Speed
W	Load

Contents

List of Figures

List of Tables

1
Introduction

This Chapter introduces the thesis by outlining the background of the study, the main objectives, and the scope and limitations of the work.

1.1 Background

International shipping plays an important role in the global economy, accounting for approximately 90% of global trade. The maritime industry is adopting strategies to reduce its environmental impact by adopting new regulations for sustainable practices. According to the International Maritime Organization (IMO) and the United Nations Conference on Trade and Development Agency (UNCTAD), which are responsible for the regulation of shipping, it is stated that international maritime transport accounts for approximately 3% of global carbon dioxide (CO_2) emissions produced by industrial and human sources (IMO, 2020).

To address this environmental challenge, the IMO has introduced more regulations (European Commission, 2025). This strategy outlines long-term goals to achieve net-zero greenhouse gas (GHG) emissions from international shipping by 2050. This objective aligns with Sustainable Development Goal 7 of the Paris Agreement and the Sustainable Development Goals of the United Nations. This goal focuses on gaining access to affordable, reliable, sustainable and new types of energy. (United Nations, 2025).

The 2023 IMO GHG Strategy introduces indicative checkpoints to help track progress toward reducing carbon emissions. According to IMO (2023a), the strategy aims to reduce CO_2 emissions in international shipping by at least 40% by 2030, around 80% by 2040, compared to 2008 levels, and net-zero emissions by or around 2050 IMO (2023b). Additionally, in 2030 the shipping industry should be using zero or low-emission technologies and fuels for at least 5% of its total energy, aiming for 10% (United Nations Conference on Trade and Development, 2024).

To achieve this objective, the 2023 IMO GHG Strategy IMO (2023a) includes innovation in vessel design to obtain higher energy efficiency and the adoption of alternative propulsion systems. A current area of investigation is the use of wind-powered ships, an approach with historical roots in early maritime navigation that is being reconsidered due to recent advances in technology and engineering. Wind-assisted ship propulsion (WASP) technologies have gained increasing attention in

recent years as viable tools to reduce our dependence on fossil fuels and minimize emissions.

1.1.1 Types of wind propulsion

Flettner rotors were invented in 1929 by Anton Flettner. He developed spinning vertical cylinders that, by using the Magnus effect, generate propulsion. Recognized by figures like Albert Einstein, in 1924, an experimental rotor vessel, the MS Buckau prototype, had more efficiency over traditional sails, offering up to 90% fuel savings and lower crew needs. However, rotor sails did not become commercially popular due to low fuel costs and high installation expenses. Since 2015, the increasing global focus on reducing emissions and improving energy efficiency has resulted in higher interest in wind-assisted propulsion and brought Flettner's concept back into consideration for modern maritime applications. (Thies & Fakiolas, 2022)

Mechanical sails are systems designed to generate thrust by using wind power through shaped surfaces that move in a controlled manner. These systems operate based on these aerodynamic principles:

- Accelerated airflow over the sail surface
- Controlled pressure distribution
- Boundary layer management
- Adaptable geometry

Flow acceleration can be achieved by leading a high wind speed across the sail surface. This can be performed through fast rotation, for example, in Flettner rotors, which also influence the surrounding pressure distribution, or by guiding the system through the wind in a controlled manner, as seen in kite technologies.
Some configurations improve efficiency by managing the boundary layer using methods such as suction, as found in suction wingsails. Others improve aerodynamic efficiency by adjusting their geometry by extending flaps or altering the sail's shape to better adapt to wind conditions.

Flettner rotors

Flettner rotors consist of a composite rotor, support tower, bearing foundation, an electric variable-speed drive system, wind sensors, and a control panel. The support tower extends about two-thirds of the rotor's height and transfers forces to the deck. Rotation is achieved via an electric motor with a variable frequency drive. When the Flettner rotor sail is exposed to wind, the cylinder creates a pressure differential across the sides, generating lift perpendicular to the wind flow and drag in the wind direction, as described in Figure 3.1. (Thies & Fakiolas, 2022)
The size of the rotor typically ranges from 18 to 35 meters in height and 2 to 5 meters in diameter. Flettner rotor efficiency is affected by its aspect ratio (height to diameter) and rotational speed. Higher aspect ratios and larger projected areas improve efficiency, but air draft limitations must be considered. Key constraints

include high power requirements at high speeds, installation space limitations, and aerodynamic interference between rotors. To reduce these effects, rotors should be spaced at least six times their diameter apart, ideally more than twelve times. (Lu & Ringsberg, 2020)

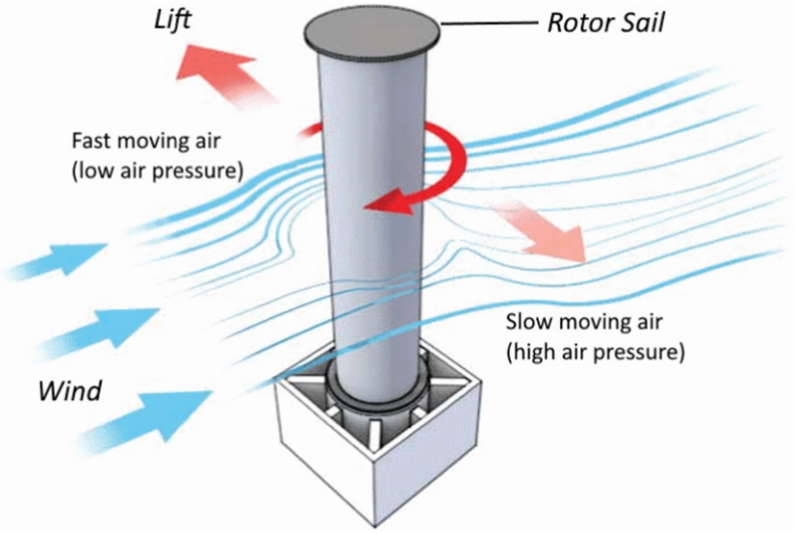

Figure 1.1: Flettner rotor (Thies & Fakiolas, 2022).

Wingsails

Wingsails use aerodynamic lift to generate thrust. They have a hard aerofoil structure installed on the deck of ships in a vertical position. Wingsails can be shaped like aircraft wings in cross-section, providing high stability and efficiency across a range of wind conditions. They can be constructed from lightweight materials such as composite fibers. (Thies & Fakiolas, 2022)

Wingsail designs typically follow two main approaches: cambered profiles and multi-element systems. In this thesis, the cambered profile from Zhu (2024) is used. This design can increase flow separation and structural loads Zhu et al. (2023a). Multi-element sails, such as those in the Oceanbird concept, shown in Figure 1.2, consist of a main wing and movable flaps that adjust the camber to gain efficiency and optimize the lift. This setup improves lift over a wider range of wind angles but requires more precise control and complex mechanics (Thies & Fakiolas, 2022). Zhu et al. (2023a) investigated the lift and drag characteristics of a crescent shaped airfoil and observed that the crescent shape generates significantly larger thrust force compared to a NACA0015 airfoil.

Figure 1.2: Wingsail from Oceanbird (Oceanbird, 2025).

The efficiency of the wingsails depends on the orientation relative to the apparent wind to maximize the lift-to-drag ratio (Zhu, 2024). According to Thies and Fakiolas (2022), a wingsail system can reach a lift coefficient (C_L) of 2.5 to 3.0 under an optimal angle of attack. Flettner rotors reach a maximum C_L of 12–13 (Thies & Fakiolas, 2022). Therefore, wingsails generally require a larger surface area to generate equivalent thrust. The power consumption for sail adjustments is relatively low (0.5–5 kW) (Thies & Fakiolas, 2022). However, physical constraints, such as available deck space, air draft limitations, structural requirements, and interactions with ship operations, must be carefully considered. Wingsails are best suited for large vessels like tankers or LNG carriers (Zhu et al., 2023a). This thesis focuses on crescent-shaped wingsail design due to its aerodynamic benefits and practical advantages, including easier manufacturing, reduced maintenance, and simpler operation compared to other wind propulsion technologies.

Suction wingsails

The suction wingsail was first developed in the 1980s by Jacques Cousteau and his team under the name Turbosail. Unlike rotor sails or conventional wingsails, suction wingsails are a stationary structure with an internal system that controls the boundary layer of the wingsail to actively manage the airflow around the profile to obtain a higher aerodynamic performance. These sails are vertically mounted on the deck of the ship. The cross-section of the wingsail has an oval shape and large thickness. The ventilator system is located inside the wingsail near the top of the structure, which draws in air through surface openings distributed along the vertical span. This powered suction smooths the turbulent boundary layer, to prevent flow separation and improve lift while reducing drag. The suction wingsail can reach a C_L of 5-6. (Thies & Fakiolas, 2022)
Power consumption varies depending on the sail size, ranging from 7.5 to 15 kW. Compared to rotor sails, suction wingsails offer higher aerodynamic performance without the complexity and structural reinforcement required for rotating systems. (Thies & Fakiolas, 2022)

This design includes a fixed or movable trailing edge flap to further improve performance, particularly in low wind speeds or less favorable wind directions. The sail can pivot on the vertical axis to align with the apparent wind. (bound4blue, 2025)

In Figure 1.3, a representative video frame from Oceanbird illustrates the aerodynamic configuration of the suction sail. The image shows how the wind flow remains attached to the sail to generate high lift.

Figure 1.3: Aerodynamic operation of the bound4blue suction sail concept (bound4blue, 2025).

The airborne towing kite

The airborne towing kite is an innovative wind propulsion system developed by German researchers in the late 1990s. This type of wind propulsion is mainly based on drag forces for propulsion, which optimizes its performance under downwind conditions. The towing kite is a rope system connected and operated air-inflated elliptical-shaped aerofoil that flies in the air to capture wind energy from high altitudes, generating forward thrust for ships. The towing kite operates at elevations ranging from 150 to 400 meters, where wind conditions are stronger and more stable. (Thies & Fakiolas, 2022)

The system consists of several integrated components. The main element is the flying kite, which generates aerodynamic lift. It is connected to the vessel via a high-strength synthetic towing rope, which transmits the generated force. A control pod, located between the kite and the rope, governs the kite's motion using a network of suspension lines attached to its edges and surfaces. The launch and retrieval of the kite are handled by a towing winch, and a reefing winch assists with docking maneuvers. A telescopic mast assists with the kite's deployment and retrieval, and the system is powered by an electro-hydraulic power pack. The automated operations are controlled by software that responds to real-time wind and ship conditions. (Thies & Fakiolas, 2022)

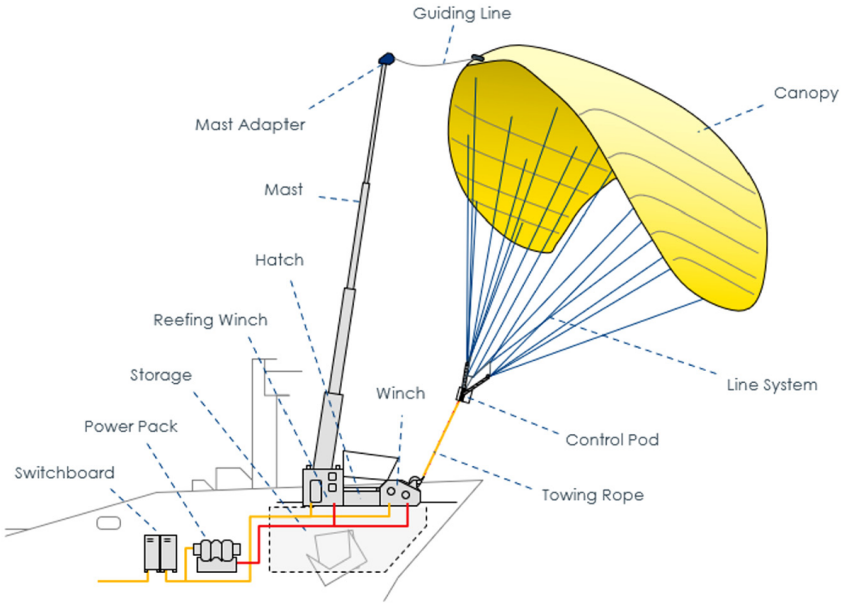

Figure 1.4: A propulsion kite system- Wind propulsion, SkySails (Thies & Fakiolas, 2022).

The kite first ascends to a neutral zenith position, where it is stable but does not produce towing force. To generate a towing force, the kite flies in an 8-shaped trajectory through the air. This dynamic movement increases the apparent wind speed acting on the kite, generating higher lift and thrust. The kite achieves optimal performance in the power zone as shown in Figure 1.5, at elevation angles between 10° and 35° above sea level. (Thies & Fakiolas, 2022)

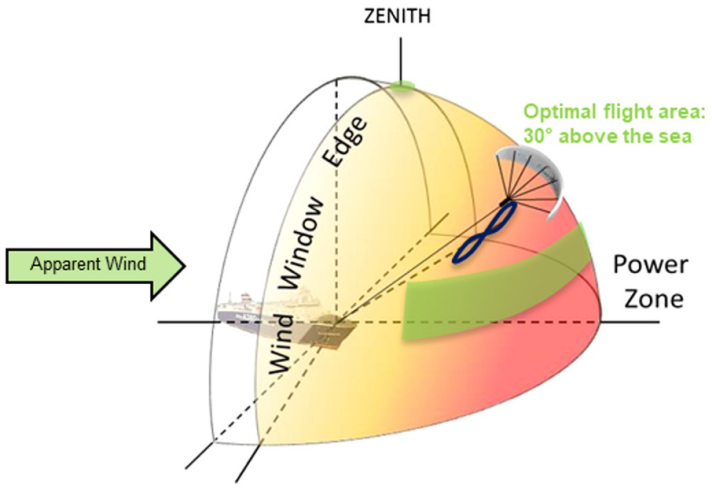

Figure 1.5: Wind window of a propulsion kite- Wind propulsion, Airseas (Thies & Fakiolas, 2022).

The kite's lift coefficient rates from 0.8-1.2, having a surface area between 400 m^2 and 600 m^2 (Thies & Fakiolas, 2022). Studies and operational data suggest that the

airborne towing kite can be 2 to 5 times more efficient than traditional on-deck wind propulsion systems according to Thies and Fakiolas (2022). Container ships, LNG carriers, Ro-Ro ferries, and cruise ships are suitable for this type of wind propulsion.

1.2 Objectives

The goal of this master's thesis is to investigate the aerodynamic interactions and fluid-structure interaction (FSI) effects arising from the use of multiple wingsails on ships. The study focuses on applying two-way coupled FSI methods to analyze the complex flow fields generated by wingsail interactions and to evaluate their impact on both propulsion performance and structural response. To achieve this goal, three objectives are set:

- Apply two-way coupled FSI simulation techniques and investigate the aerodynamic complexities introduced by wingsail interactions and the resulting structural effects
- Model and analyze the interaction between multiple wingsails
- Quantify the extent of wingsail interaction and assess its influence on propulsion efficiency and structural behavior

1.3 Scope and delimitations

This thesis investigates the aerodynamic and FSI effects between multiple crescent-shaped, cambered wingsails installed on a ship. The work focuses on understanding the aerodynamic performance and structural response under idealized controlled conditions to ensure a clear and manageable research scope.

To this end, the following delimitations are adopted:

- Wind gradient effects are not considered. A uniform horizontal inlet flow is assumed in both CFD and FSI simulations to isolate the fundamental aerodynamic behavior. Although real-world conditions are recognized to involve complex vertical wind profiles due to air-sea interactions and vessel motion, such dynamics are beyond the scope of this study.
- The hull-wingsail interaction is excluded. Aerodynamic and structural analyzes are performed without accounting for interference effects from the hull or superstructures of the ship. This simplification allows for a focused investigation on the wingsails themselves, independent of vessel-specific geometries.
- To reduce computational complexity in the two-way coupled FSI simulations, the internal structure of the wingsail is modeled using a simplified representation. The structural materials are assumed to behave in a linear elastic manner, which means the effects of plastic deformation are excluded from the scope of this study.

1.4 Outline of the thesis

This thesis is divided into six Chapters. In Chapter 1, a brief introduction is provided along with objectives and scope. Chapter 2 contains literature review. The theory relevant to this project is discussed in Chapter 3. The methods used are presented in Chapter 4. In Chapter 5 the results are analyzed and discussed. Chapter 6 contains the conclusions.

2
Literature review

This Chapter provides information about the current state of knowledge of crescent-shaped wingsail. The review aims to identify existing technologies and methodologies related to crescent-shaped wingsails, focusing on a numerical analysis perspective.

2.1 Aerodynamic analysis

To evaluate the overall performance and the propulsive efficiency, it' fundamental to perform an accurate assessment of the aerodynamic loads acting on the wingsail. The interaction between wind flow and the surface of the wingsail influences its propulsion capacity. Theoretical methods are based on certain assumptions, which can limit their applicability to complex real-world scenarios. For instance, predicting aerodynamic performance during stall conditions, where significant flow separation occurs, remains challenging for these approaches. Empirical methods provide approximate estimations for fluid flow problems. Wingsails are a relatively new innovation, and their design and operational history are limited. Consequently, the empirical techniques used to assess their propulsive performance are still in the early stages of development.
Previous studies state that crescent-shaped profiles offer a higher thrust force coefficient, and are easier to operate when the wind direction changes from the starboard side to the port side under the downwind condition. (Zhu et al., 2023b)

2.1.1 Experimental method

Experimental methods on wingsails focus on evaluating aerodynamic performance and understanding flow phenomena such as separation and vortex shedding. Burden et al. (2010) and Hua et al. (2012) studied multi-wingsail systems with elliptical designs resembling crescent shapes. Their findings demonstrated improved aerodynamic efficiency compared to traditional arc-shaped profiles. A current limitation is the lack of high-Reynolds-number validation for cambered wingsails. Crescent-shaped profiles tend to experience flow separation even at low angles of attack (Zhu, Chernoray, et al., 2024). The sensitivity of the body behavior creates a challenge in interpreting wind tunnel results for full-scale performance (Zhu, 2024).

Zhu (2024) conducted a series of wind tunnel (WT) experiments to validate numerical simulations and investigate aerodynamic performance under controlled con-

ditions. The tests were conducted at Chalmers University of Technology in the Laboratory of Fluids and Thermal Science using a closed test section equipped for detailed aerodynamic measurements.

Figure 2.1: WT test setup (Zhu, 2024).

The models tested in Zhu, Chernoray, et al. (2024), were scaled at 1:100, constructed from aluminum, with a chord length (L_c) of 0.14 m. The distance between the rotational axis of each sail in the triple model is 1.5 L_c. The three sails were mounted on a rotating platform to obtain precise control of the angle of attack and the yaw angle. The model test results confirmed that the crescent-shaped wingsail generates significant thrust under various wind speeds and angles of attack. The middle sail and the sail situated on the right in Figure 2.1, which as simplification is called back sail, experience changes in flow conditions due to the wake and downwash created by the front wingsails, resulting in reduced thrust. The front wingsail, which is situated on the left in Figure 2.1 provides the best propulsive performance.(Zhu, Chernoray, et al., 2024) The results show superior aerodynamic behavior of crescent-shaped wingsails compared to conventional symmetric airfoils such as NACA0015, particularly at moderate angles of attack (15°–20°) Zhu, Chernoray, et al. (2024), where the lift reached its maximum. In Zhu, Chernoray, et al. (2024), the aerodynamic interactions between sails led to asymmetric load distributions, where the front sail experienced the highest forces.

2.1.2 Numerical method

Numerical methods can resolve complex flow behaviors with high resolution in both space and time accuracy. Computational fluid dynamics (CFD) simulation utilizes

fluid mechanics principles to analyze fluid motion. These simulations require high computational power to capture real-world interactions between aerodynamic forces and structural deformation. By applying numerical methods, the governing equations are divided into smaller sections, allowing for accurate predictions and insights into complex fluid interactions, thereby enhancing the understanding of physical systems. CFD uses 3D designs from CAD software to analyze well-known model parameters, providing insights into material properties. While CFD results may not be exact, they closely approximate the model's behavior, allowing for the development of real designs based on these approximations. (Atoyebi & Ojo-Kupoluyi, 2024)

Early computational studies, Ouchi et al. (2011) and Ouchi et al. (2013), conducted 3D Reynolds-averaged Navier–Stokes RANS simulations on a nine-wingsail configuration. Other researchers, Nikmanesh (2021) and Zhu, Yao, and Ringsberg (2024), used unsteady RANS (URANS), models to study time-dependent aerodynamic responses and inform design optimization. However, most of the previous investigations focused on low Reynolds number (Re) applications. (Zhu, 2024)

Zhu, Yao, and Ringsberg (2024) employed URANS to evaluate the performance of such profiles and found them to have a higher performance than conventional NACA 0015 foils in thrust generation. However, it describes more pronounced flow separation to unsteady features like tip vortices. To extend this work, Zhu, Yao, and Ringsberg (2024) compared URANS and Improved Delayed Detached Eddy Simulation (IDDES) results, demonstrating that although both methods agreed on time-averaged loads, IDDES offered superior accuracy in capturing transient vortex phenomena. To validate the findings, Zhu (2024) also conducted wind tunnel tests at moderate Reynolds numbers ($Re \sim 10^5$) and identified force coefficients around transition regions, effects that are not observable in traditional symmetric airfoils. Zhu, Chernoray, et al. (2024) studies used a hybrid turbulence modeling framework based on the k–ω SST model, implemented mesh refinement near separation and wake regions.

FEA is a numerical method that approximates how physical systems behave under various conditions. By breaking down complex structures into smaller elements, FEA simulates the response of each element under specified conditions. The results provide valuable insights into the overall performance of the design. To investigate the aerodynamic performance of crescent-shaped wingsails, a key objective of this research is to understand their structural responses under aerodynamic loading. Finite Element Analysis (FEA) is used to evaluate the stress and strain distribution, determine the eigenfrequencies, and capture the dynamic deformation of the wingsail structures. These analyses are essential to ensure that the wingsails can withstand complex aerodynamic forces encountered during operation. (Zhu, 2024)

3

Theory

3.1 Principle of sailing

The oldest and simplest type of sailing is sailing with the wind. When the wind is coming from behind, it is considered downwind sailing (Kimball, 2010). Sailing downwind versus upwind, considering how the wind appears, is quite different. This is due to the apparent wind speed, V_{AW}, which by definition is the wind speed as observed by someone on the moving boat. The true wind speed, V_{TW}, is the speed of the wind relative to the water and V_S, is the boat speed relative to the water. For downwind sailing, the apparent wind speed is

$$V_{AW} = V_{TW} - V_S \tag{3.1}$$

Sailing upwind is possible because of the generation of lift. This is feasible since the aerodynamic force on the sail is not parallel with the wind direction, and likewise, the hydrodynamic force from the water is not aligned with the boat's motion relative to the water. These forces combined, create a net forward motion. By combining the lift generated from both the wind and the water, the boat is able to sail upwind (Kimball, 2010).

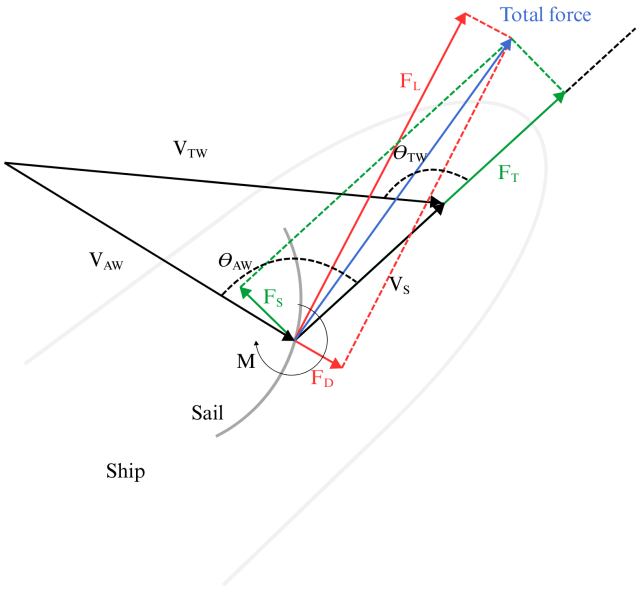

Figure 3.1: Principle of sailing.

Apparent wind angle, θ_{AW}, as can be seen in Figure 3.1, is the angle between the ship's speed, V_S, and the apparent wind speed, V_{AW}. The apparent wind angle varies between 0° and 180°, 0° when the wind is coming from ahead and 180° when the wind is coming from astern. The true wind angle, θ_{TW}, is the angle between the direction the true wind is coming from and the direction the boat is moving at. The range of the true wind angle is the same as for the apparent wind angle regarding from which direction the wind is coming and in what direction the ship is headed. The apparent wind speed and the apparent wind angle can be calculated using equations 3.2 and 3.3 (Zhu, 2024).

$$V_{AW} = \sqrt{V_S^2 + V_{TW}^2 + 2V_S V_{TW} \cdot \cos\theta_{TW}} \tag{3.2}$$

$$\theta_{AW} = tan^{-1}\left(\frac{V_{TW} \cdot \sin\theta_{TW}}{V_S + V_{TW} \cdot \cos\theta_{TW}}\right) \tag{3.3}$$

Points of sailing refer to the angles a boat sails relative to the wind. When the wind comes directly ahead (within 45° of the bow), the sail cannot generate lift, creating a no-go zone where boats must tack to sail upwind.

In Figure 3.2, the various points of sailing are presented, which refer to the course of the boat in relation to the wind. In the no-go zone, the boat is not able to sail, and the sail will be luffing. When sailing close-hauled, or upwind, the sails are hauled in to the stern corner of the boat as flat as possible while still having draft to propel the boat. The concept of tacking is utilized in this position to sustain its voyage meaning that the boat is zigzagging at angles of approximately 45° from the wind's axis. The next position is the close reach position, where the sails are almost close-hauled. The position after that, beam reach, is generally considered to be the fastest angle to sail at. At the broad reach position, the ship is sailing slightly more downwind, and therefore sails need to be let out a bit further than at the beam reach. (Bisbee et al., 1995)

The external loads on the sail are the forces and moment. The lift force (F_L) and drag force (F_D) are defined in relation to the apparent wind direction while the thrust force (F_T) and the side force (F_S) are defined in relation to the ship's sailing direction (Zhu, 2024). When wind or water exerts force on an object in the direction it is moving, this phenomenon is referred to as drag. Lift acts perpendicular to drag, exerting a force that is essential to understanding aerodynamic principles (Kimball, 2010). According to (Guzelbulut et al., 2024), crescent-shaped airfoils rely on lift-based thrust generation, which leads to increased thrust and therefore reduced required propulsive power. The thrust can be calculated using Equation 3.4 (Zhu, 2024).

$$F_T = F_L \cdot \sin\theta_{AW} - F_D \cdot \cos\theta_{AW} \tag{3.4}$$

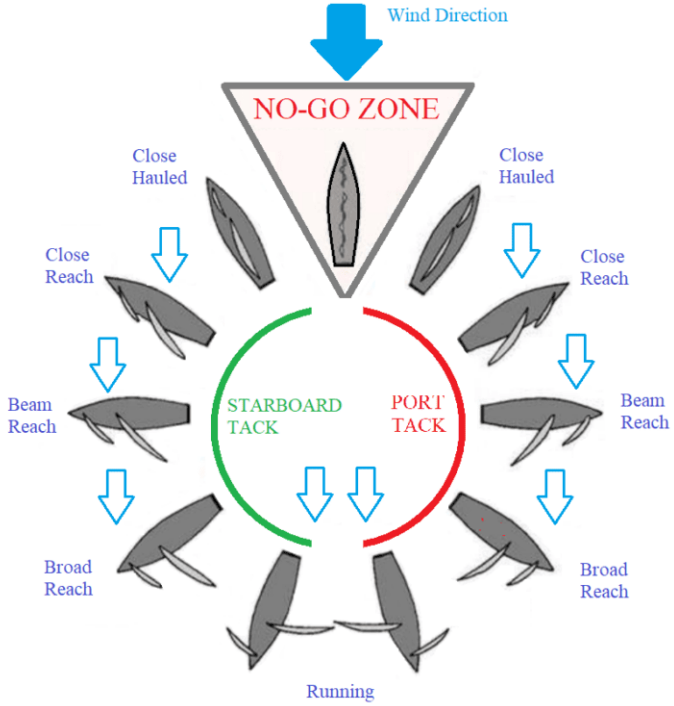

Figure 3.2: Points of sailing.

3.2 Thin airfoil theory

The angle of attack (AoA) is a crucial parameter in three-dimensional aerodynamic models. It is conventionally defined as the angle between the chord line of an airfoil and the wind velocity vector, see Figure 3.3 (2011, Wind Energy Systems T. Maeda, G. Schepers).

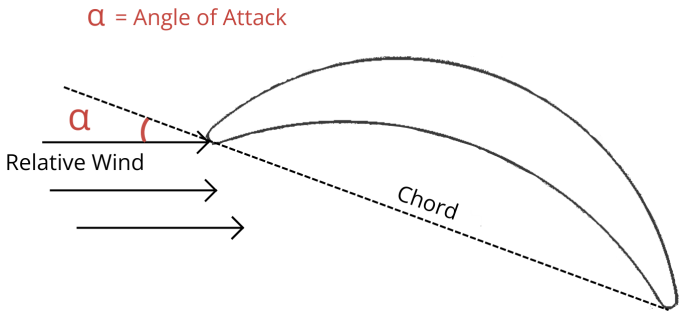

Figure 3.3: Angle of Attack is the angle between the chord line and the relative wind vector.

Thin airfoil theory (TAT) is an essential principle of aerodynamics which enables predictions about how wing-like shapes, or airfoils, interact with airflow to generate lift and other aerodynamic effects (Leishman, 2025). TAT models flow over a stationary airfoil using a vortex sheet in a potential flow (T. Liu et al., 2023). It imposes the Kutta condition at the trailing edge to calculate lift and moment. TAT

is based on the assumption that a vortex sheet approximates a boundary layer as viscosity approaches zero, with its strength equaling the circulation that generates lift (T. Liu et al., 2023). Figure 3.4 shows the representation of the vortex sheet as a boundary layer.

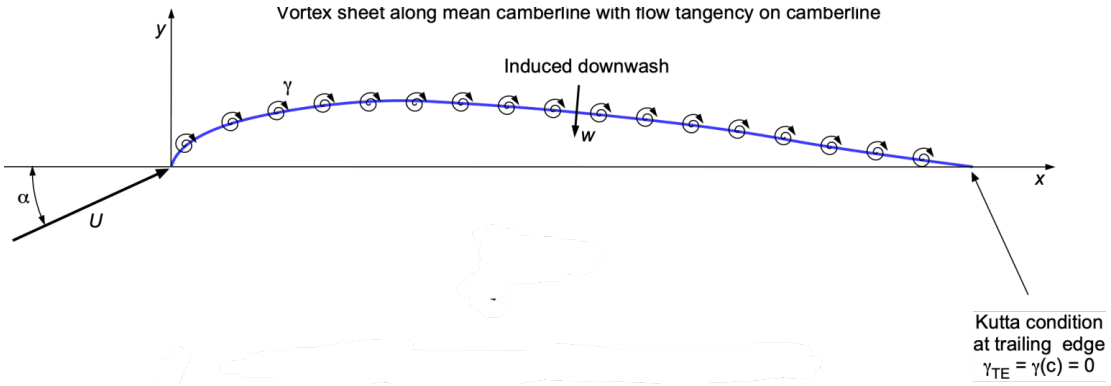

Figure 3.4: Representation of thin airfoil theory where the vortex sheet is on the chord line and Kutta condition is being met at the trailing edge (Anderson, 2023b).

When describing the lifting force with Bernoulli's law, one must first examine the stagnation point near the leading edge. A stagnation point suggests that the velocity at this point is zero. Outside the airfoil's boundary layer, flow velocity increases, causing a pressure drop and suction over the upper surface. This change results from mass conservation, compressing streamlines above the stagnation point. Circulation, defined as the line integral of velocity around a closed curve, is crucial for lift. Without circulation, the rear stagnation point unrealistically sits above the trailing edge. Real flows shed a starting vortex that increases circulation and shifts the stagnation point to the trailing edge, satisfying the Kutta condition for sharp-edged bodies in steady flow. Figure 3.5 shows an airfoil and the flow field around it, illustrating the Kutta condition being met and not met, with the shift in stagnation point marked in red on the drawing. (Kuethe & Chow, 1997)

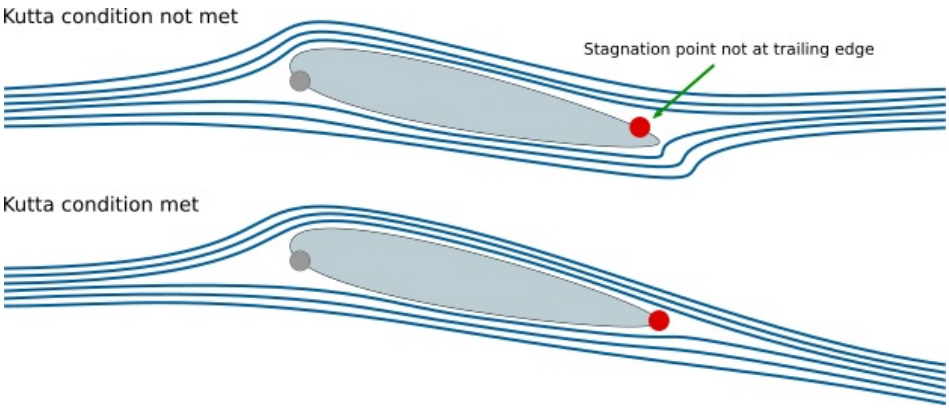

Figure 3.5: Kutta condition (Stack Exchange, 2017).

The vortex theory of a lifting airfoil, developed by Lanchester and Prandtl, predicts airfoil characteristics regardless of geometry. They replaced the physical wing with a

system of vortices that create airflow similar to the actual flow. The developed vortex system was divided into the bound vortex, the starting vortex, and the trailing vortex, see Figure 3.6. The starting vortex and trailing vortex systems are physical entities, while the bound vortex is a hypothetical arrangement of vortices that replaces the real physical lifting surface, such as an airfoil, in every aspect except for thickness (Y. Liu et al., 2023).

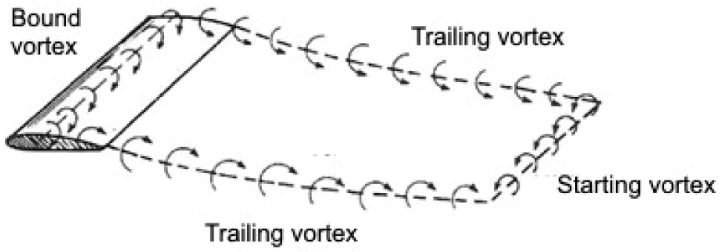

Figure 3.6: The three types of vortices, trailing vortex, starting vortex, and bound vortex around an airfoil (Y. Liu et al., 2023).

The total vortex system of the lifting body, along with its bound vortex system, creates a complete ring that adheres to physical laws. While the starting vortex dissipates quickly, the bound vortex and trailing pairs on either side form the horseshoe vortex system, see Figure 3.7. (Y. Liu et al., 2023)

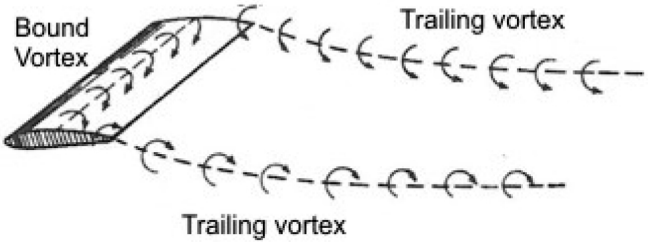

Figure 3.7: Representation of the horseshoe vortex system (Y. Liu et al., 2023).

Wingtip vortices are circular patterns of rotating air generated by a wing as it produces lift. Also known as trailing or lift-induced vortices, they can occur at various points, not just at the wingtips. These vortices contribute to induced drag and downwash, reflecting the complexities of three-dimensional lift generation. Figure 3.8, shows the tip vortex on the drawing. (Clancy, 1975)

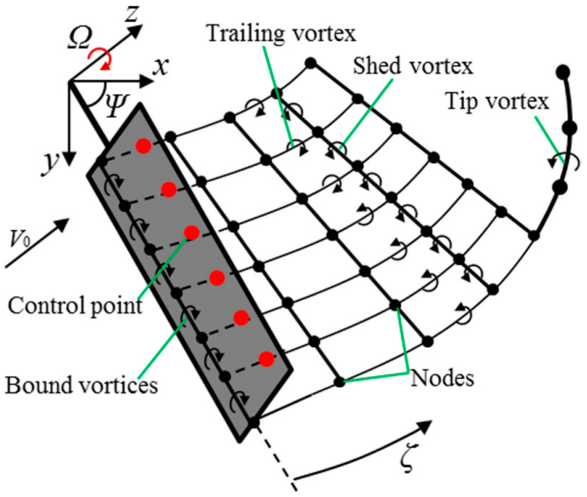

Figure 3.8: Drawing of an airfoil with marked vortices Xu et al., 2018.

3.3 Boundary layer

The nonlinear partial differential equations describe all general flow fields and are called the Navier-Stokes equations. In their non-dimensional form, these equations depend on the Reynolds number, which indicates the impact of viscosity on the flow. The higher the Reynolds number, the lower the viscosity effects are on the flow. Boundary-layer theory applies to the Navier-Stokes equations at high Reynolds numbers, exposing two distinct flow regions: an inviscid flow field and a narrow region near the wall called boundary layer. (Schlichting & Gersten, 2017)
Figure 3.9 illustrates the boundary layer concept developing over an airfoil's upper and lower surfaces. In this region, viscosity effects are significant, impacting the aerodynamic characteristics of the airfoil or any body. It is important to note that boundary layers are thinner in reality than depicted in the figure, and they grow in thickness and other properties as they progress downstream. (Anderson, 2023a)

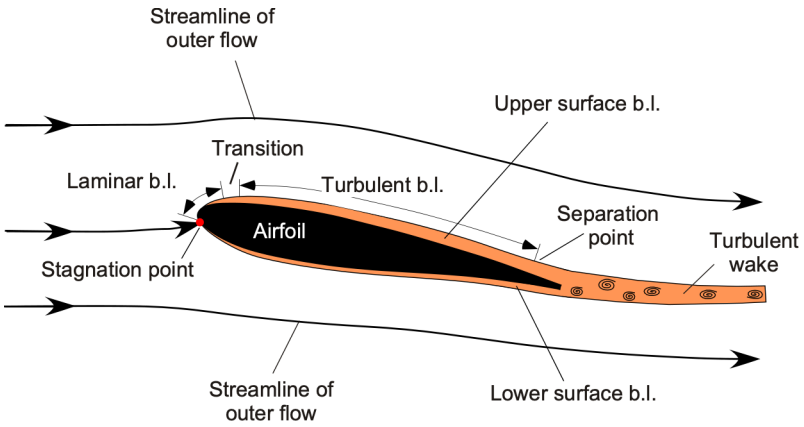

Figure 3.9: Representation of the boundary layer developing over the upper and lower surfaces of an airfoil at moderate to high Reynolds number conditions (Anderson, 2023a).

Laminar flow occurs when fluid particles move in one direction with minimal perpendicular movement. Turbulent flow involves particles moving perpendicularly, forming swirls called eddies, see Figure 3.10. Factors like flow rate, density, and viscosity, along with the geometry of objects, influence the transition from laminar to turbulent flow. (ANSYS, 2025)

In boundary-layer flow, the wall's pressure gradient significantly impacts the transition region's position. In areas of decreasing pressure (accelerated flow), the boundary layer typically remains laminar, while even a slight increase in pressure can induce transition. For slender bodies like airfoils, optimal body shape and pressure distribution can delay the transition point, reducing friction drag by nearly half in laminar airfoils. Additionally, suction techniques can further influence the transition zone's position, thereby minimizing drag. Transition experiments and direct flow simulations help investigate nonlinear transition processes and the effects of free stream disturbances, such as sound waves or turbulence, which impact the transition region's characteristics. (Schlichting & Gersten, 2017)

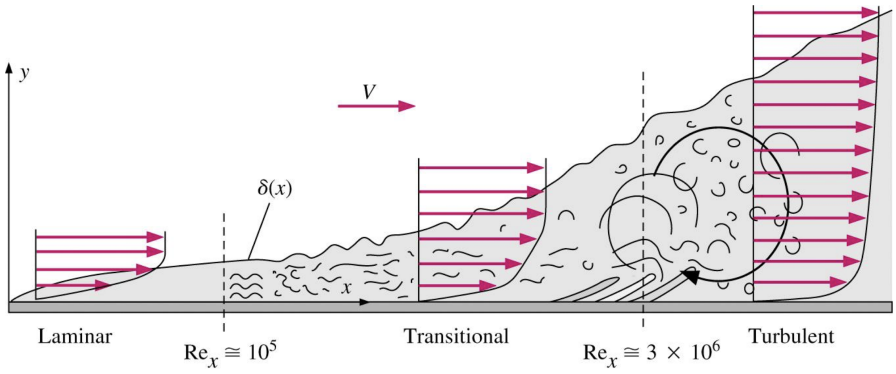

Figure 3.10: Laminar-turbulent transition representation (The Aviation History Online Museum, 2002).

3.4 Flow separation

Friction in the flow generates shear stress at a body's surface, contributing to aerodynamic drag known as skin friction drag. Additionally, friction can lead to flow separation, which creates pressure drag. Understanding flow separation is crucial for analyzing airflow over an airfoil.(Jr., 2015)

Flow separation occurs when the flow around a foil detaches, primarily due to a positive or negative angle of attack (AoA). It initiates in the boundary layer when wall shear stress reaches zero from flow deceleration, resulting in an unsteady turbulent area with recirculation zones and potential vortical structures from velocity shear and reverse flow. See Figure 3.12 for a visualization of this process. (Cabeza, 2022)

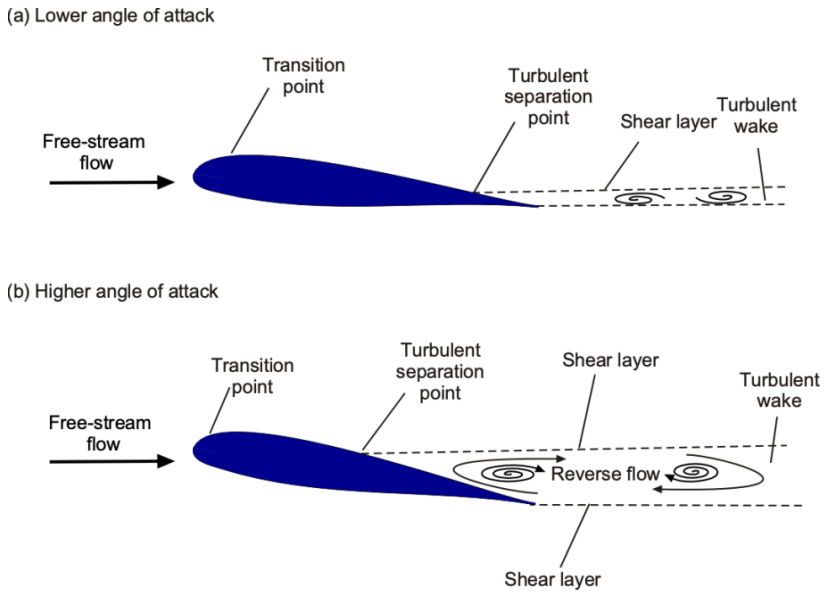

Figure 3.11: Flow about an airfoil section at increasing angle of attack showing the progressive forward movement of flow separation and the onset of stall (Anderson, 2023a).

In a study by Eisenbach and Friedrich (2008) at a high angle of attack (18°) and Re = 10^5, the flow over the NACA4415 airfoil was analyzed. Results showed flow instability due to an adverse pressure gradient, leading to boundary layer separation shortly after the suction peak. A transitional separation bubble formed between 4% and 18% of the chord, where laminar flow transitioned to turbulence. This turbulent shear layer drew in higher-momentum freestream fluid, allowing for downstream reattachment. However, a second turbulent separation occurred near 70% of the chord due to a stronger adverse pressure gradient, creating a large recirculation zone past the trailing edge. Large-eddy simulation (LES) effectively captured these features, revealing unsteady behavior with vortex formation in the trailing-edge region. The presence of both leading-edge and trailing-edge separation zones illustrates the complex flow dynamics at high angles of attack. (Eisenbach & Friedrich, 2008)

According to Zhang and Wang (2022), the study on the NACA0012 airfoil at low Reynolds numbers shows that flow separation creates a separation bubble near the leading edge. As the angle of attack (AoA) increases, the unstable shear layer forms discrete vortices that periodically detach from the bubble, causing unsteady vortex shedding that affects wake dynamics. Shedding frequency rises with the growing separation bubble due to the merging of large-scale vortices. This alternating shedding generates oscillating lift and drag forces on the airfoil. Further increases in AoA lead to different shedding regimes, indicating the sensitivity of vortex dynamics to angle and Reynolds number. These changes in flow structure and stability directly impact aerodynamic performance and must be considered in unsteady flow modeling. (Zhang & Wang, 2022)

Von Kármán vortex streets are patterns of swirling vortices formed when a fluid

flows past a bluff object, like an island or mountain. As the fluid separates around the object, it alternately sheds vortices, creating spirals visible from satellites. First explained by Theodore von Kármán, this phenomenon involves fluctuating pressures generating oscillating forces on structures. The object's size and fluid speed determine the spacing and frequency of the vortex shedding. (Wunderground, 2025)

Figure 3.12: Karmán vortex street created by a cylindrical object where the flow on opposite sides of the object is given different colors, showing that the vortices are shed from alternating sides of the object (Wikipedia contributors, 2025).

3.5 Cantilever beam theory

A cantilever beam is a structural element that extends horizontally, supported at only one end, see Figure 3.13. The unsupported end, known as the cantilever, extends beyond the support point. These beams are commonly used in construction for balconies, roofs, and overhangs.

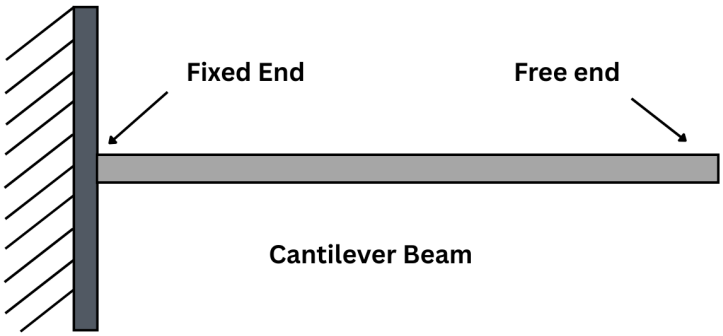

Figure 3.13: Cantilever beam.

Based on the beam theory, the wingsail is modeled as a cantilever beam since the wingsails are assumed to be installed on a fixed deck without any motion (Zhu, 2024). There are a range of equations for calculating cantilever beam forces and deflections. There are different types of loading condition relevant for wingsails exposed to wind forces such as point load, distributed load and moment. These can

be simplified into cantilever beam formulas as can be seen in Figure 3.14. In the equations presented in Figure 3.14 the W stands for load, L for member length, E for Young's Modulus and I for the beam's moment of inertia.

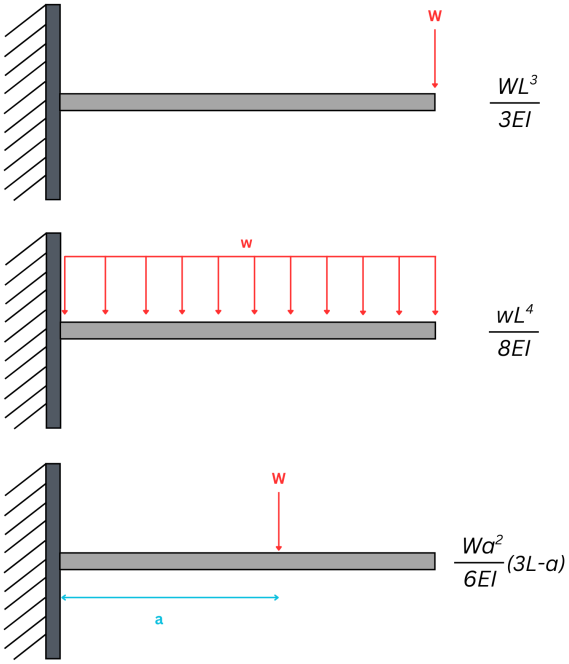

Figure 3.14: Cantilever beam.

3.6 Flutter and vortex induced vibration

Flutter and vortex induced vibration (VIV) are two types of flow-induced vibrations (FIV) observed in external flows (Nakamura et al., 2013).

VIV is an example of a fluid-structure interaction, Laboratory of Fluid Mechanics and Instabilities (LFMI) (2025) and is a result of vortex shedding (Singh & Mittal, 2023). Vortex shedding comes from instabilities in the wake Singh and Mittal (2023), and this process is largely influenced by the geometry of the body, its orientation to the incoming flow as well as the Reynolds number (Berger & Wille, 1972). Interaction between the fluid flow and motion of the structure can either enhance or diminish the shedding of vortices (Singh & Mittal, 2023). In can also alter the vortex shedding pattern and in certain extreme cases, this interaction can initiate vortex shedding in an otherwise steady flow or suppress it completely (Singh & Mittal, 2023). VIV should be either avoided (e.g. when vibrations are damaging to the structural integrity of a structure such as bridges) or enhanced (e.g. in energy harvesting systems where the oscillatory motion caused by VIV can be converted into usable energy)(Laboratory of Fluid Mechanics and Instabilities (LFMI), 2025).

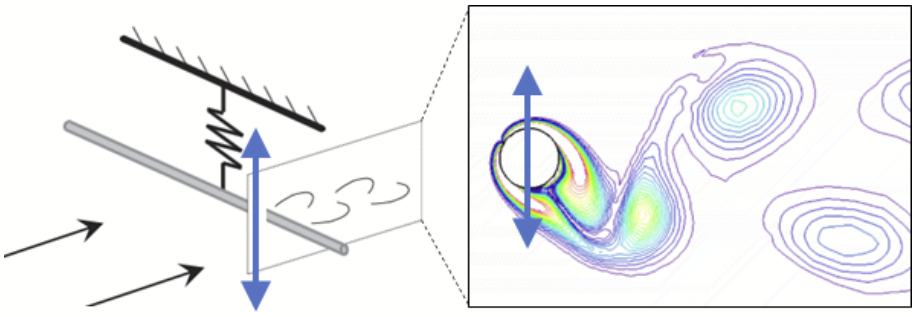

Figure 3.15: VIV model (on the left) and vortex shedding during high-amplitude VIV (Laboratory of Fluid Mechanics and Instabilities (LFMI), 2025).

Flutter is a dangerous phenomenon encountered in flexible structures which are subjected to aerodynamic forces such as aircraft, buildings, and bridges (Hebert et al., 2025). It occurs as a result of interactions between aerodynamics, stiffness, and inertial forces on a structure (Hebert et al., 2025). When the shape of an elastic structure changes relative to the free-stream flow, it modifies the fluid forces acting on the structure, which causes the system to move further away from equilibrium (Singh & Mittal, 2023). For airfoils, as wind speed rises, there might occur a point where structural damping fails to control motions intensified by added aerodynamic energy (Hebert et al., 2025). This event can lead to structural failure, making the consideration of flutter characteristics essential in cases where flexible structures experiencing aerodynamic forces (Hebert et al., 2025). Unlike VIV, flutter develops from fluid-elastic instability and involves minimal exchange of energy between the filament and the fluid (Singh & Mittal, 2023). Flutter responses occur not as often as VIV responses, and while VIV amplitudes peak at lower speeds, flutter responses increase as the speed decreases (Singh & Mittal, 2023). Systems can exhibit both VIV and flutter together (Singh & Mittal, 2023).

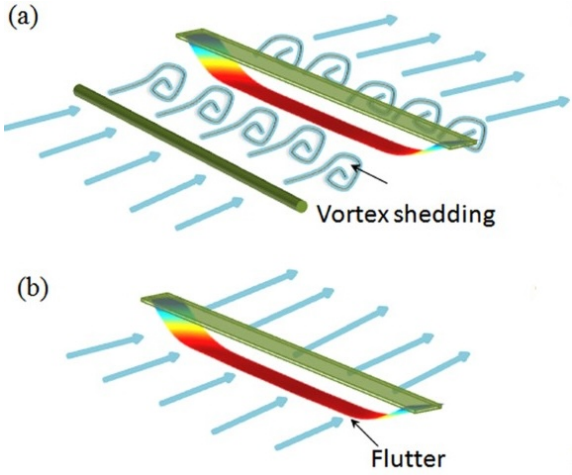

Figure 3.16: The schematic of the (a) vortex induced vibration; (b) flutter phenomenon (Chen et al., 2016).

4

Methods

This Chapter presents the methods utilized in this thesis. In this thesis, the aerodynamic and aeroelastic performance of crescent-shaped wingsails is studied. Prior to the simulation, a literature review was conducted, where numerical simulation was analyzed, focusing on existing studies about CFD, FEA and FSI. The software used in this study was STAR-CCM+, and the preliminary simulation file was created by Zhu (2024), which contained the design and mesh setup for one crescent shaped wingsail. That was expanded to a three wingsail setup. The simulation model was then modified, using CFD and FEA to simulate the interaction between fluid flow and structural response for three wingsails. The simulation included different conditions to examine the aerodynamic and structural interactions between the wingsails. The results of these simulations were then analyzed to quantify the effects of wingsail interactions on propulsion performance and structural responses.

4.1 Wingsail Geometry and Configuration

The geometry of the wingsail is made up of arcs and circles and the shape is controlled by the chord length (L_c), edge radius, suction-side arc radius, and mast diameter. The parameters are suggested by ScandiNAOS AB according to its practice. For this thesis, L_c is 14 m, and the edge radius is 0.2 m. The profiles are labeled "DxRy," where "x" stands for the mast diameter and "y" for the suction-side arc radius. For the profile "D2R8," the mast diameter is 2 m and the suction-side arc radius is 8 m, which results in an arc radius of 10.6 m on the pressure side (Zhu, 2024).
The real wingsail features a telescopic function, as shown in Figure 4.2. It has three configurations based on wind conditions: fully expanded, semi-retracted, and fully retracted. Each sail is divided into four sections and can be expanded at low wind speeds, while it can be semi- or fully retracted to prevent structural failures at high wind speeds. The fully expanded height is 74 m, and the fully retracted height is 26 m. The height of the mast section between the wingsail bottom and the deck is 4 m.

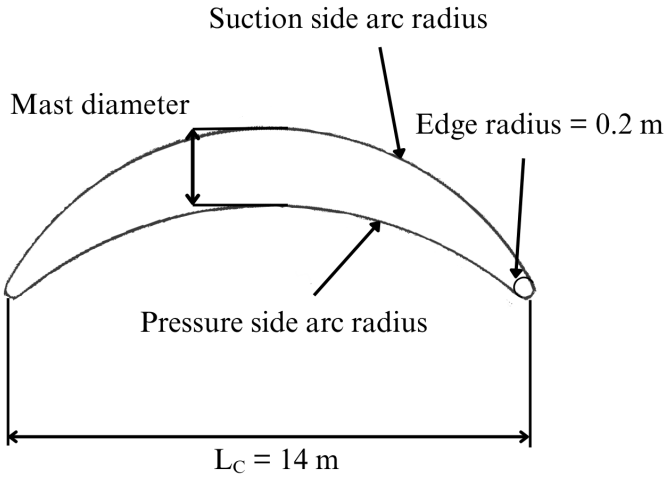

Figure 4.1: Important geometries of the crescent shaped wingsail used in this thesis including parameters suggested by ScandiNAOS AB.

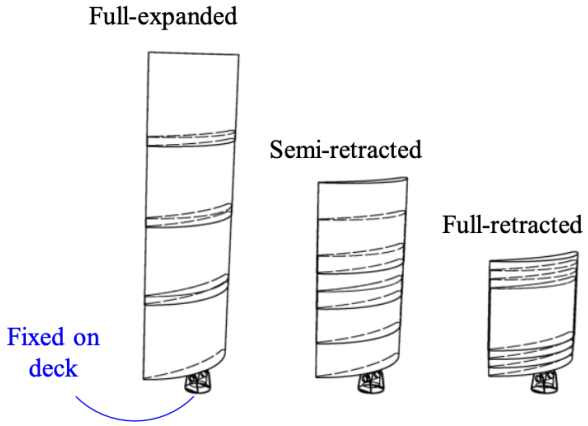

Figure 4.2: Three telescopic functions presented, full-expanded, semi-retracted as well as full-retracted (Zhu, 2024).

Multiple wingsails are installed on ships to capture additional wind power (Zhu, 2024). Figure 4.3 shows a triple-sail system with three wingsails installed along the centerline of the ship. The distance between the mast centers is suggested by industry experts at ScandiNAOS AB and is 1.5 L_c. For simplification when discussing the sails in this thesis, the sail closest to the bow is referred to as "Sail F", or front sail, the middle sail as "Sail M" and the sail closest to the stern, "Sail B" or back sail.

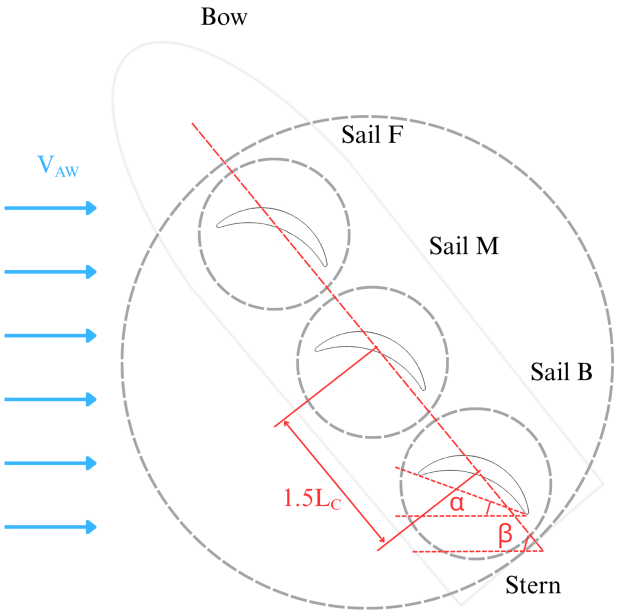

Figure 4.3: Setup of three wingsails on a vessel.

In this thesis, three cases of apparent wind angles are observed with a fixed angle of attack at 20° since that angle generates the most thrust according to Zhu (2024). The three AWA's studied are 60°, 90° and 120°.

4.1.1 Coordinate systems

In this study, the Cartesian coordinate system is used following the previous studies Zhu, Chernoray, et al. (2024). The origin is located at the center of the bottom surface of the middle wingsail. The X-axis is aligned with the streamwise direction as shown in Figure 4.4.

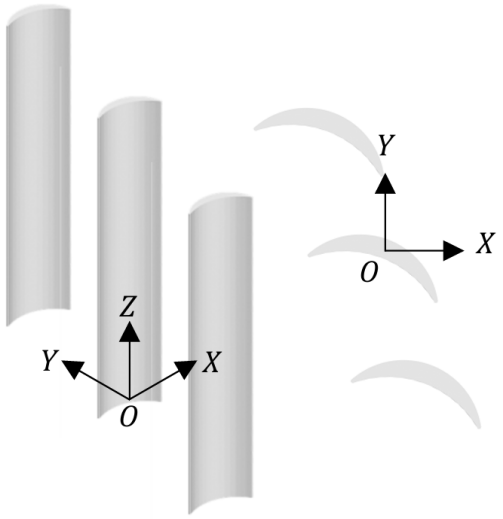

Figure 4.4: Coordinate systems of the triple-sail (Zhu, Chernoray, et al., 2024).

4.2 CFD

CFD simulations are utilized to compute flows in this study, which employs mesh generators and solvers from STAR-CCM+.

4.2.1 Domain and boundary conditions

Figure 4.5 shows the cuboid computational domain that is used in the numerical simulation. The dimensions of the computational domains were verified by Nikmanesh (2021), where the distance between the sail's top end and the domain's top boundary is 4 times the sail's spanwise length. This setup evaluates realistic flow features, e.g. for tip vortices. A no-slip boundary condition is applied at the wingsail walls. The domain inlet features a velocity inlet boundary condition with a uniformly distributed flow speed (8 m/s), corresponding to the apparent wind speed. The side boundaries and outlet are configured with a pressure outlet boundary condition where the pressure loss coefficient is set as zero.

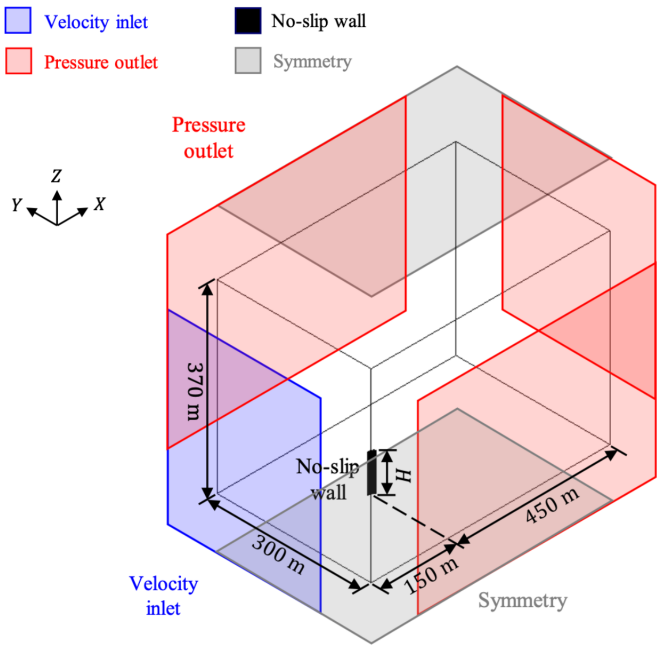

Figure 4.5: Computational domain used in this thesis, expanded to three wingsails, but with the same diameters (Zhu, 2024).

4.2.2 Mesh setup

The meshes used for this simulation are unstructured meshes with trimmed cell topologies. The number of cells used is 40 million. Figure 4.6 shows a top view of the mesh setup for the "symmetry bottom and freestream tip" configuration. The sizes of each cell for each refinement can be seen in Figure 4.6 and the cells maintain a uniform size in each region. Both the regions near the foil and the wake are refined for more accurate results of the fluid in that area. In addition, a cylindrical

volumetric mesh refinement is near the foil, with diameter 1.4 L_C, or 19.6 m. As flow separation points are expected to distribute around the edges, refinement is applied near the edges, as Figure 4.7 shows.

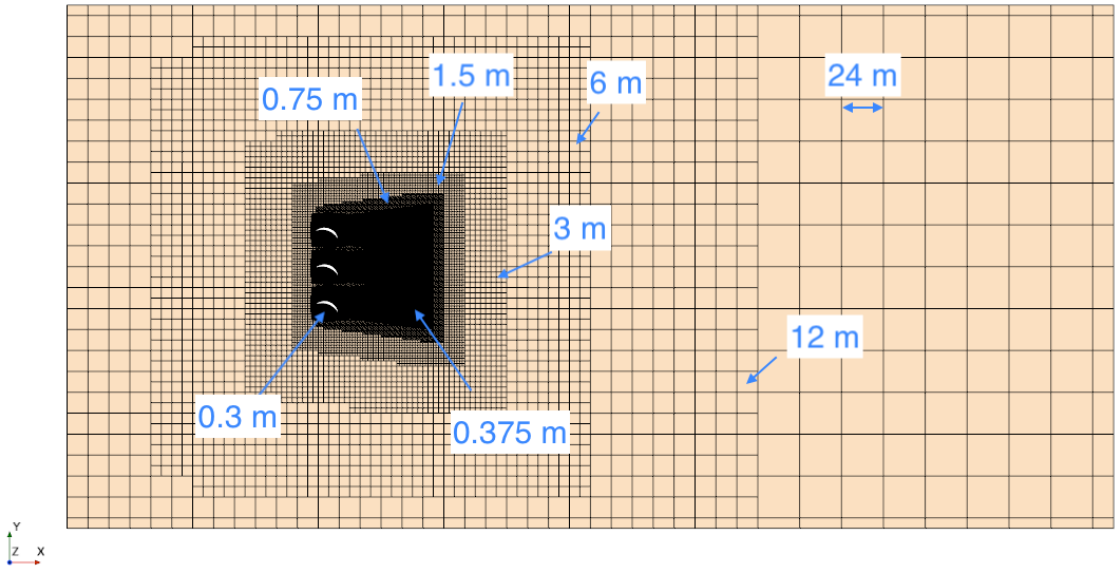

Figure 4.6: An unstructured mesh for the crescent-shaped wingsails with cell sizes in each region.

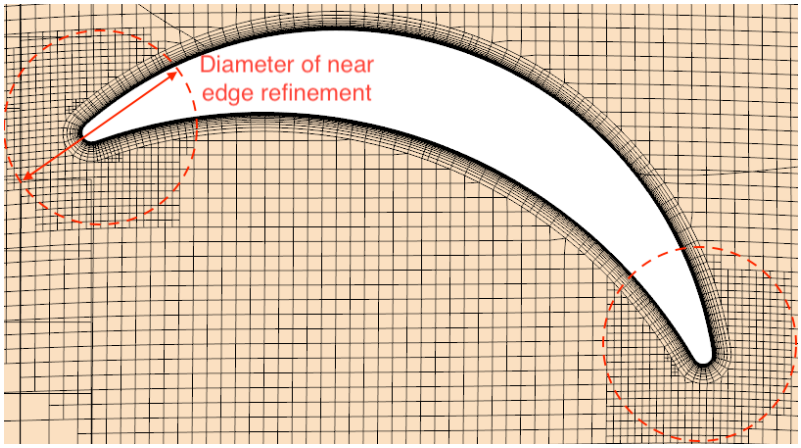

Figure 4.7: Mesh structure for near edge refinement.

Prism cells are generated to resolve the boundary layers. The total absolute thickness of the prism layer is 0.4 m, the near-wall thickness of the prism layer is 0.005 m and the total number of prism layers is 14. The $y+$ value was set to be less than 5. Figure 4.8 shows the diameters and the prism layers from the simulations.

4.2.3 Turbulence modeling strategies: URANS and IDDES

Nikmanesh (2021) stated that crescent-shaped wingsails are prone to strong flow separation and as a result from that, turbulence increases. Therefore, structural

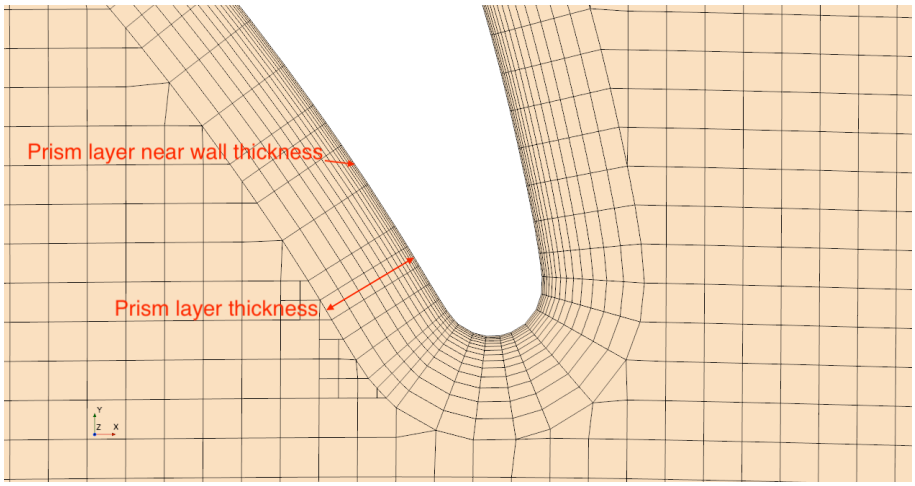

Figure 4.8: Mesh structure around the wingsail and the prism layers.

vibrations induced by vortices are increased. To account for this, it is important to simulate the turbulence. To accurately simulate the turbulence, IDDES, a DES (Detached Eddy Simulation) method is used. For both IDDES and the URANS simulations, the $k-\omega$ SST turbulence model is applied. The blended wall treatment approach is also applied to both turbulence models which offers the advantage in accounting for complex geometries and adapts to the local y+. For cases that have high Reynolds number, the laminar-turbulent transition can take place at an early stage which leads to turbulence-dominated boundary layer. To prevent this, transition models are not applied in high Reynolds number simulations for full-scale wingsails. (Zhu, 2024)

4.2.4 Discretization strategy and solver settings

In this thesis, the flow is assumed to be incompressible due to the low freestream Mach number. The finite volume method (FVM) is applied to discretize the governing equations. In the simulations, an implicit scheme with a segregated flow solver based on the SIMPLE algorithm is implemented. A hybrid second-order upwind and bounded-central scheme are used to discretize the convection fluxes on cell faces. On internal and boundary cell faces, the diffusion fluxes are discretized with a second-order scheme. For the second-order hybrid Gauss-LSQ method, it involves the reconstruction of field values at cell face since it's applied in gradient computation. This method includes the secondary gradients of the diffusion fluxes as well as the pressure gradients and the rate-of-strain tensors used in the turbulence model. To discretize the time derivative, a second-order implicit method is applied and Reichardt law utilized for the momentum equations. (Zhu, 2024)

4.3 FEA

In this study, a dynamic FEA approach was used. The simulations utilize simplified solid models that accurately replicate the bending stiffness of the actual wingsail,

while incorporating reduced geometric complexity to improve computational efficiency.
The structural design of the actual wingsail is highly complex. The simulation uses a simplified solid model that preserves the same bending stiffness, represented by the product of Young's modulus (E) and the moment of inertia (I), as the real wingsail structure. Each section of the wingsail and mast is individually simplified for computational efficiency. (Zhu, 2024)

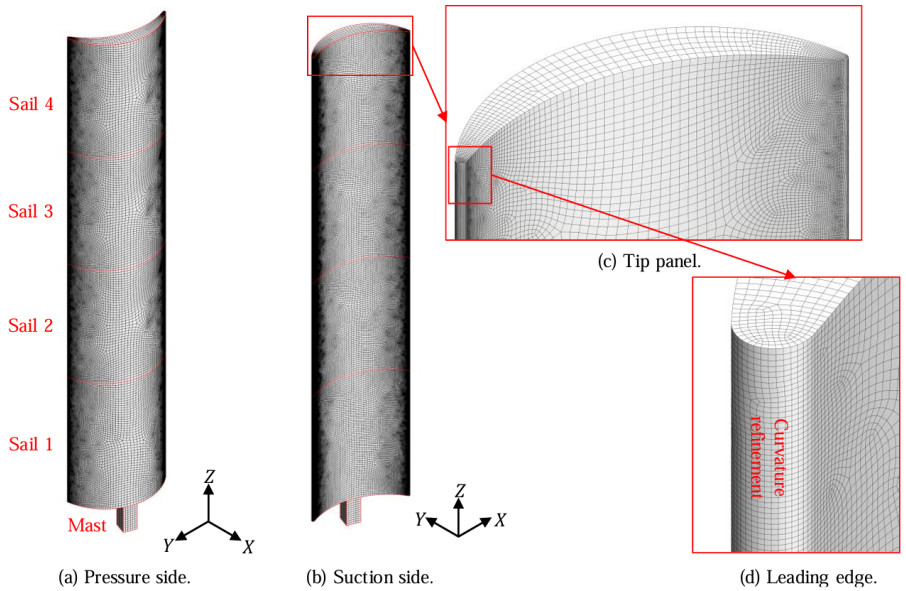

Figure 4.9: The FEA mesh with the simplified solid model (Zhu, 2024).

4.4 FSI

In FSI simulations, the coupling between the fluid and structural domains can be categorized as one-way or two-way. In Figure 4.10 illustrated by Zhu (2024), describes the solution algorithms for one-way and two-way coupled FSI simulations based on CFD for the fluid and FEA for the solid.
One-way coupled FSI focuses on the fluid forces acting on the structure, but the fluid flow is not affected by the structural response. Therefore, the simulations have a faster running time and they utilize less computational power. However, this method is limited because it does not provide accurate results in scenarios where fluid-induced deformations are significant.
Two-way coupled FSI considers the impact of structural deformation on the flow field. The fluid applies forces to the structure, leading to deformation. These structural changes influence the behavior of the fluid flow. This two-way interaction provides a more accurate representation for complex systems. However, it demands higher computational resources, as it requires the simultaneous solution of both fluid and structural equations. (Zhu, 2024)

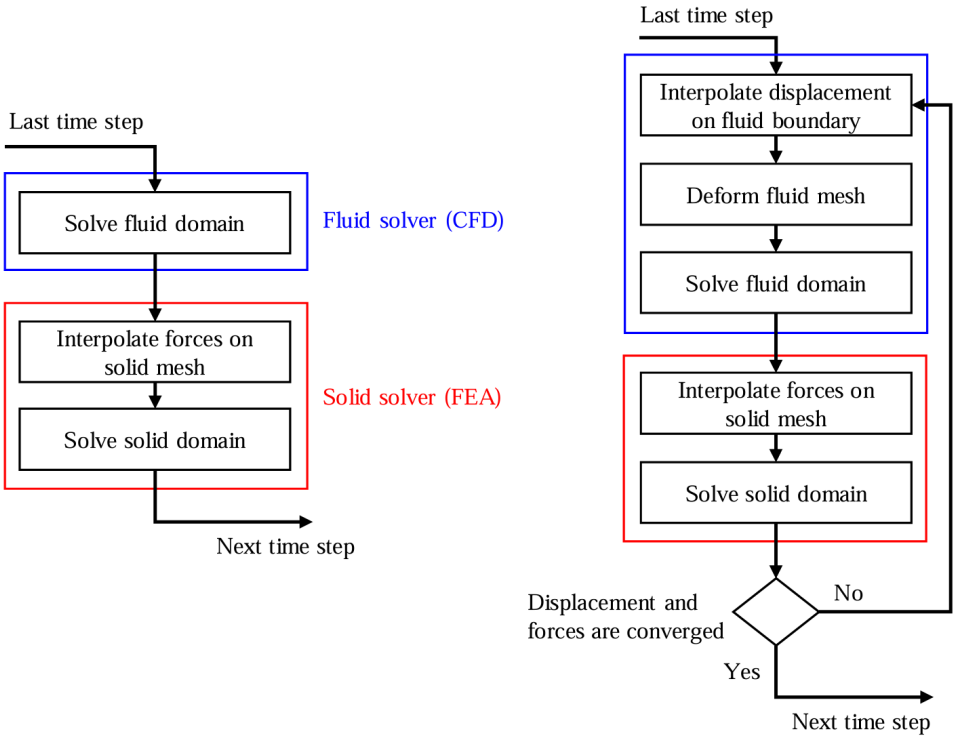

Figure 4.10: Solution algorithms for one- and two-way coupled FSI simulations based on CFD for fluid and FEA for solid (Zhu, 2024).

Two-way FSI simulations are used to capture the influence of the airflow and structural deformation. The CFD component calculates the pressure and shear stresses acting on the wingsail surface, which are then applied as external loads in the FEA solver. The resulting structural displacements are transferred back to the CFD domain, modifying the fluid mesh and updating the flow field. This exchange continues iteratively at every time step of the simulation. The Arbitrary Lagrangian–Eulerian (ALE) method is used to adapt to large deformations by allowing the fluid mesh to move with the structure without suffering excessive distortion. A conservative mapping strategy is applied to transfer physical quantities across the non-aligned fluid-solid interface, and radial basis function (RBF) morphing is used to maintain mesh quality during deformation.(Zhu, 2024)

5

Results

In this chapter, the simulation results are presented. The interaction between the flow and the three wingsails is examined using CFD and FSI simulations for different apparent wind angles. The apparent wind angle for the CFD cases is 60, 90 and 120 degrees while the apparent wind angle for the FSI is 90 degrees. The plane section for the top view is located at 3/4 of the sail, at 59.5 m from the bottom of the mast for all the simulation results.

5.1 CFD results

The CFD results will be examined for apparent wind angles (AWA) of 60, 90, and 120 degrees. All of the results are in the time frame between 47 and 60 seconds for accurate comparison. This chapter will analyze the force coefficients: lift, drag, and moment coefficients, along with the pressure distribution, velocity distribution, and turbulent kinetic energy for each AWA. A Appendix contains more detailed plots of the force coefficients. The plots there show the lift, drag and moment coefficient for each of the four sections for each sail. In all the plots, the back sail is represented in red, the middle sail is blue, and the front sail is green. What will be presented in this chapter, Chapter 5.1, will be the average coefficients for each sail, taking into consideration the length of each section as well as the total length. First the coefficients will be presented in Chapters 5.1.1, 5.1.2 and 5.1.3, then the results will be compared and discussed in Chapter 5.1.3. For AWA 60 and 120 degrees, the pressure distribution, velocity distribution and turbulent kinetic energy figures were taken at 63 seconds. For AWA 90 degrees they were taken at 65 seconds.

5.1.1 CFD lift coefficients

The following plots show the lift coefficients using the average values of the lift coefficients from each section of each sail.

Figure 5.1 shows the lift coefficients for each sail at AWA 60 deg, Figure 5.2 shows the lift coefficient for AWA 90 deg and Figure 5.3 shows for AWA 120 deg.

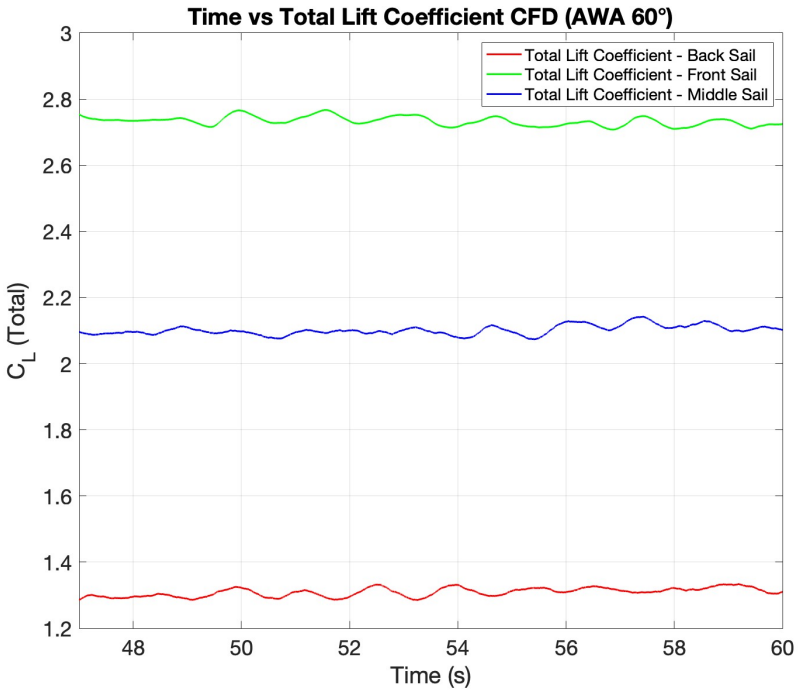

Figure 5.1: Plot showing the CFD lift coefficient for each sail in apparent wind angle 60°.

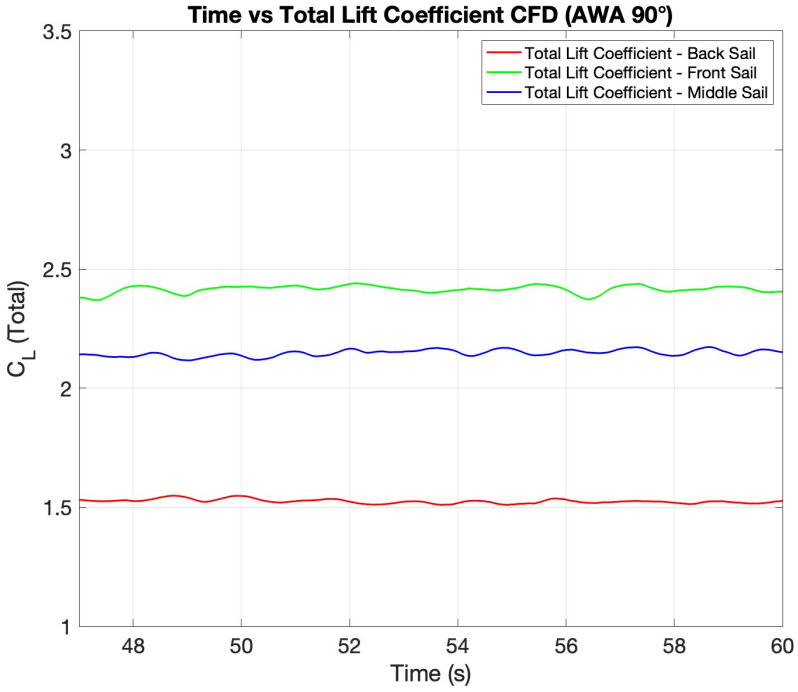

Figure 5.2: Plot showing the CFD lift coefficient for each sail in apparent wind angle 90°.

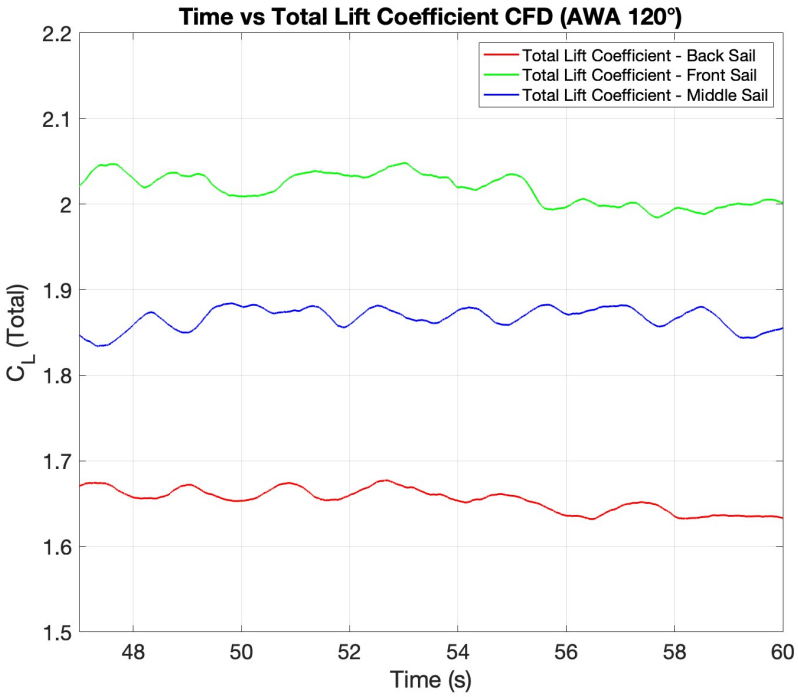

Figure 5.3: Plot showing the CFD lift coefficient for each sail in apparent wind angle 120°.

5.1.2 CFD drag coefficients

In this chapter, the drag coefficient plots are presented. Figure 5.4 shows the drag coefficient for each sail at AWA 60 degrees, Figure 5.5 shows the plot for AWA 90 degrees, and Figure 5.6 shows the plot for AWA 120 degrees. These drag coefficient plots exhibit periodic oscillations, which are likely caused by vortex shedding occurring around the sails.

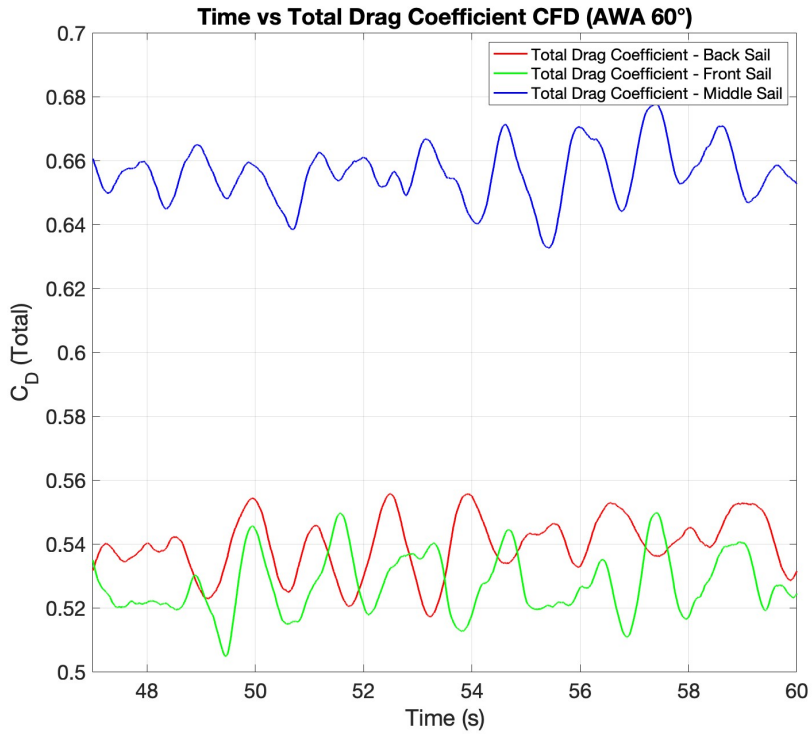

Figure 5.4: Plot showing the CFD drag coefficient for each sail in apparent wind angle 60°.

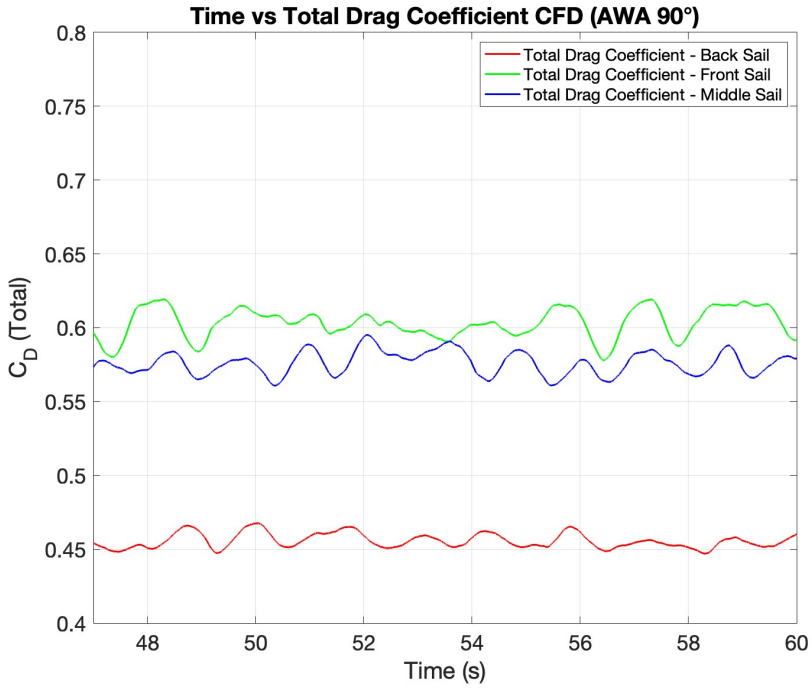

Figure 5.5: Plot showing the CFD drag coefficient for each sail in apparent wind angle 90°

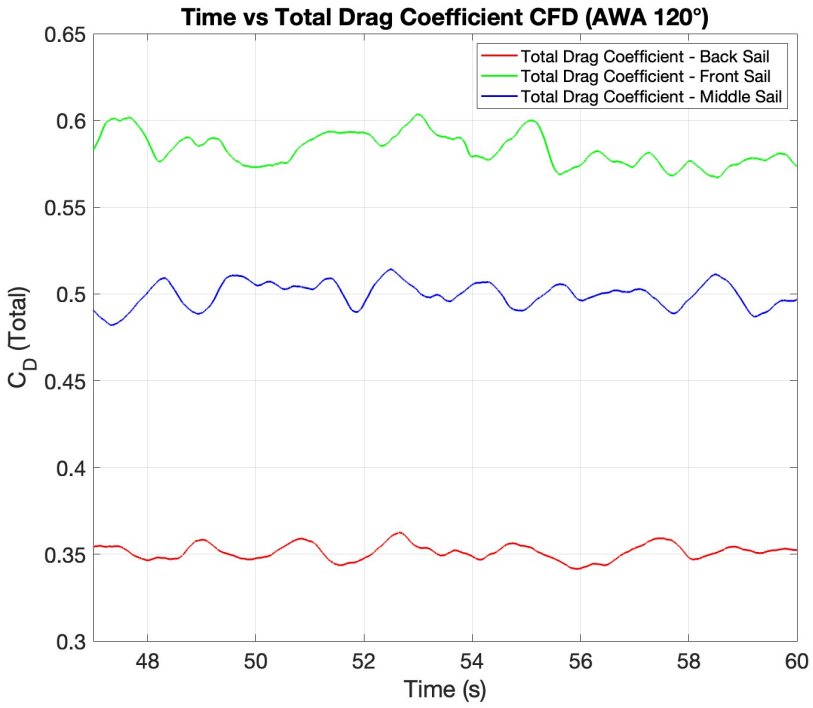

Figure 5.6: Plot showing the CFD drag coefficient for each sail in apparent wind angle 120°.

5.1.3 CFD moment coefficients

This chapter shows the moment coefficients, see Figure 5.7 for AWA 60 degrees, Figure 5.8 for AWA 90 degrees, and Figure 5.9 for AWA 120 degrees.

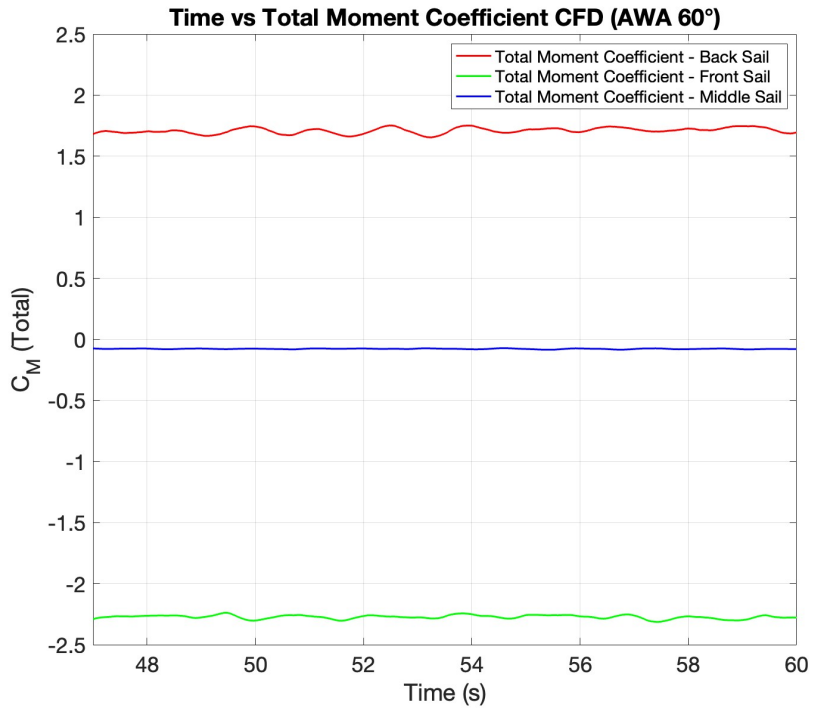

Figure 5.7: Plot showing the CFD moment coefficient for each sail in apparent wind angle 60°.

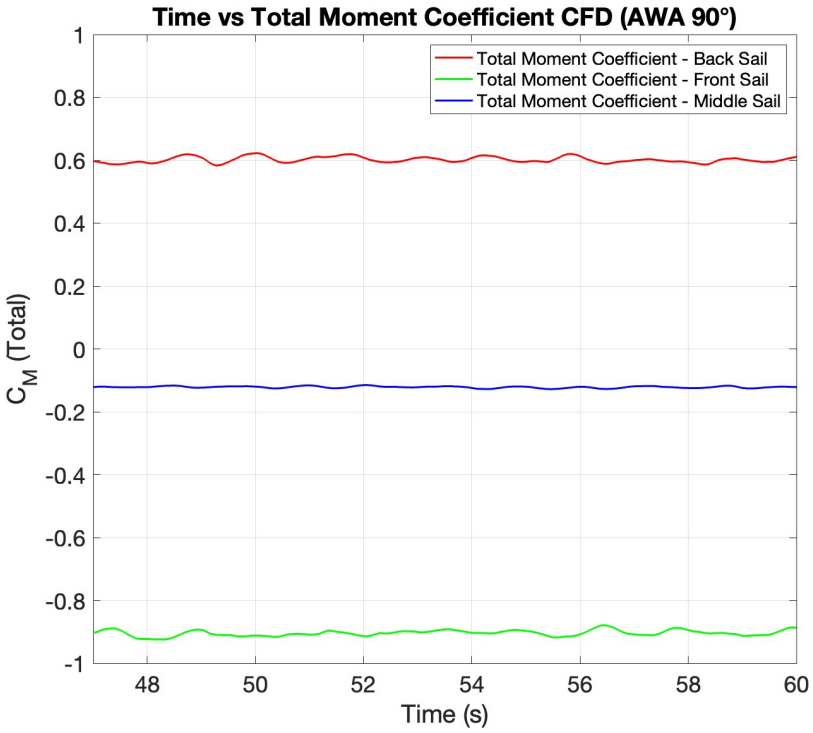

Figure 5.8: Plot showing the CFD moment coefficient for each sail in apparent wind angle 90°

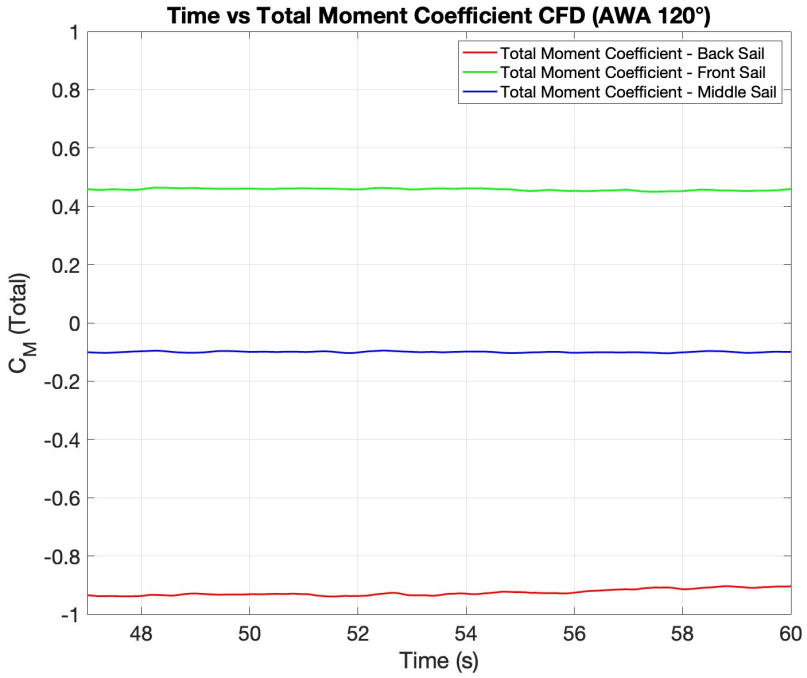

Figure 5.9: Plot showing the CFD moment coefficient for each sail in apparent wind angle 120°.

Time averaged values (CFD)

In this chapter, the time-averaged values of the force coefficients for each AWA and each sail, are presented in Table 5.1. It was visible in the plots that the lift coefficient for the front sail was always the highest and the lift coefficient for the back sail was always the lowest and the values in Table 5.1 concur with that. That is due to its undisturbed airflow and a higher pressure difference between the suction side and pressure side. If the drag coefficient is analyzed, it's the same for 90 and 120 degrees that the front sail has the highest drag and the back sail has the lowest, however for 60 degrees, them middle sail has the highest drag and the front and middle sails have very similar lower values. It can be explained since the velocity around the middle sail for AWA 60 degrees is very low compared to others, which means the pressure is a lot higher, which might result in higher drag coefficient. The moment coefficient is highly related to the pressure distribution along the suction side of the sail. A positive moment is a result of the suction being located near the leading edge and a negative moment is a result of the suction being located closer to the trailing edge on the suction side surface, as can be seen in the table and later on, on the pressure distribution figures.

A bar chart was created using the values from Table 5.1, presenting the time-average lift coefficient for the front, middle and back sail. The lift, drag and moment coefficient values are plotted on the y-axis, while the x-axis indicates the three different apparent wind angles: 60, 90, and 120 degrees. The front sail is represented in green, the middle sail in blue, and the back sail in red.

Table 5.1: Time-averaged force coefficients for AWA 60°, 90° and 120° for each sail between 47s and 60s.

		C_L	C_D	C_M
AWA 60	Sail F	2.733	0.527	-2.273
	Sail M	2.101	0.656	-0.078
	Sail B	1.309	0.539	1.709
AWA 90	Sail F	2.415	0.603	-0.904
	Sail M	2.148	0.576	-0.121
	Sail B	1.525	0.456	0.602
AWA 120	Sail F	2.018	0.583	0.458
	Sail M	1.867	0.499	-0.100
	Sail B	1.654	0.351	-0.926

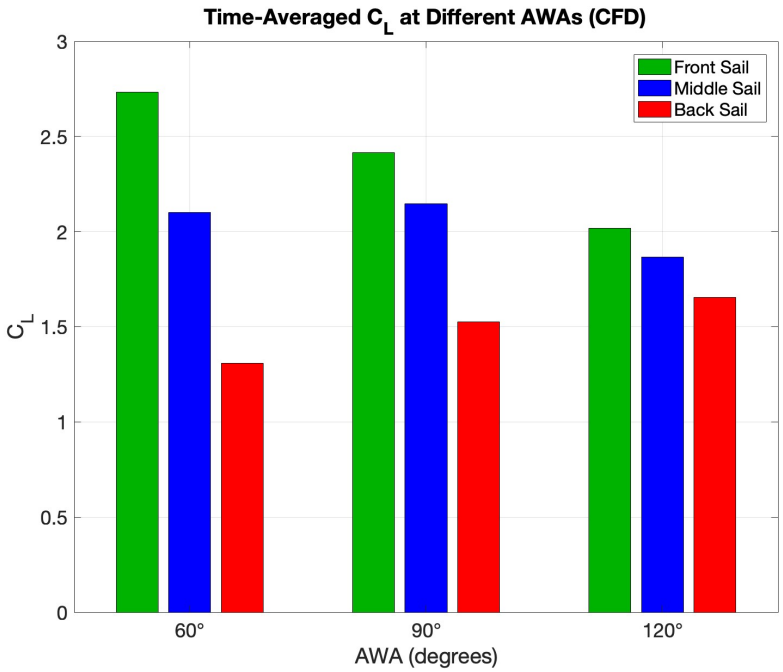

Figure 5.10: C_L at different AWA.

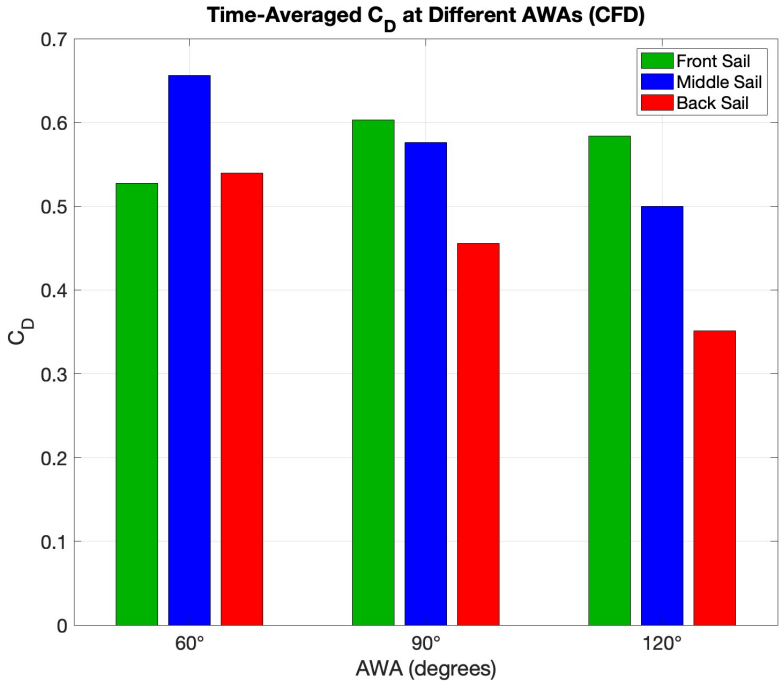

Figure 5.11: C_D at different AWA.

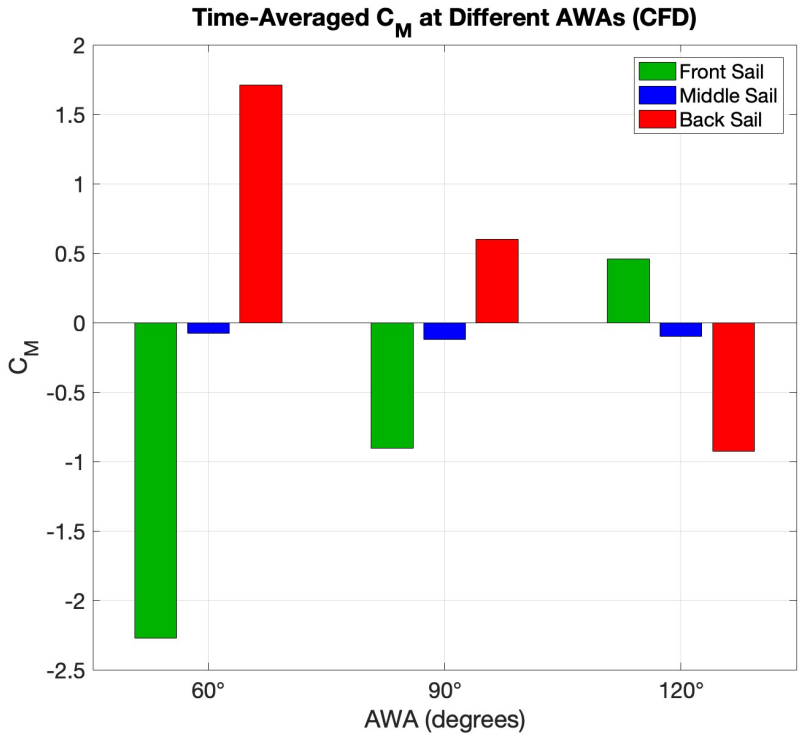

Figure 5.12: C_M at different AWA.

Table 5.2 shows the summary of the force coefficients for all sails at each AWA.

Table 5.2: Summary of the total time-averaged force coefficients of all sails for each apparent wind angle.

AWA	C_L of all sails	C_D of all sails	C_M of all sails
60 deg	6.144	1.723	-0.641
90 deg	6.088	1.635	-0.424
120 deg	5.540	1.435	-0.568

The overall lift coefficient of all sails decreases as the AWA increases. At an AWA of 60º, the sails function near optimal conditions. However, at an AWA of 120º, their efficiency decreases due to a reduced effective angle of attack, which increases flow detachment.

The overall drag coefficient of the three wingsails decreases as the AWA increases. The highest drag coefficient occurs at an AWA of 60º, while the lowest occurs at 120º.

The absolute value of the total average moment coefficient for all sails is the largest for AWA 60º and lowest for the AWA 90°.

Pressure distribution for CFD at AWA 60, 90 and 120 degrees

In this section, the pressure distribution around the wingsails is presented for different apparent wind angles with a top view of the wingsails arrangement. The color bar describes high pressure in red reaching values around 40 Pa, and low pressure in blue until approximately -160 Pa. Figure 5.13 shows the pressure distribution around the wingsails when they are at an AWA 60 degrees, figure 5.14 shows the AWA 90 degrees and Figure 5.15 shows the 120 degrees.

In the three AWA cases, the front wingsail shows lower pressure (suction) on its suction side compared to the middle and back sails. Looking at different sails, the pressure behavior varies significantly in the three cases. The front sail, at an AWA of 60º (see Figure 5.13), suction is located on the suction side near the leading edge, while on the back sail, the suction is located closer to the center of the wingsail, and even more closer to the leading edge. This is the case for AWA 60 and AWA 90 degrees, while in the case of AWA 120 degrees, the suction is located closer to the centre of the suction side and in the case of the front wingsail, it experiences a negative moment, the opposite to the other two AWA cases, meaning that more suction occurs closer to the trailing edgel. The middle and back sails, in all AWA cases, demonstrate weaker pressure gradients due to the effects of wake interference. At an AWA of 120 degrees, all sails show lower pressure gradients, indicating a reduction in aerodynamic forces.

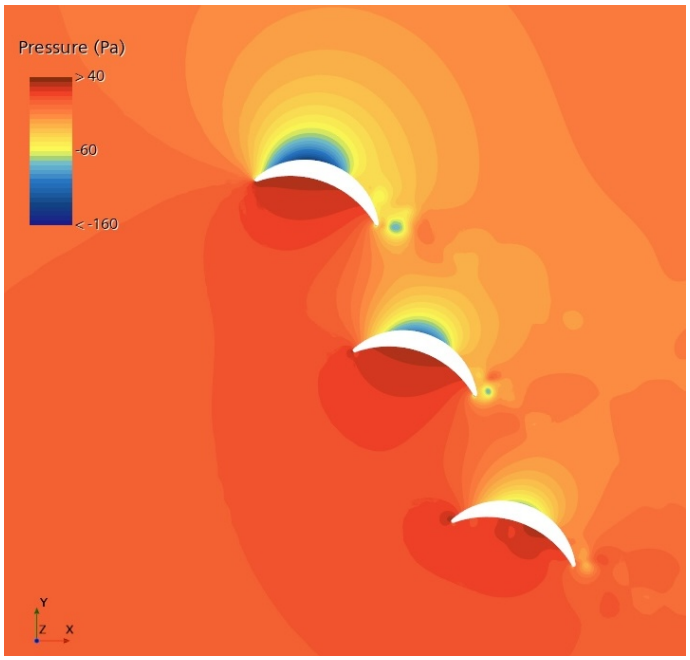

Figure 5.13: Top view of the sails showing the pressure distribution around each sail in AWA 60°.

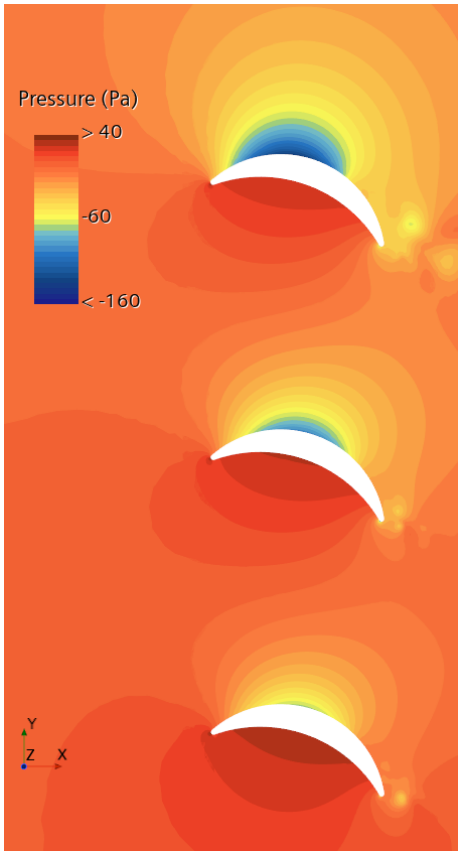

Figure 5.14: Top view of the pressure distribution of the area around each wingsail in AWA 90°.

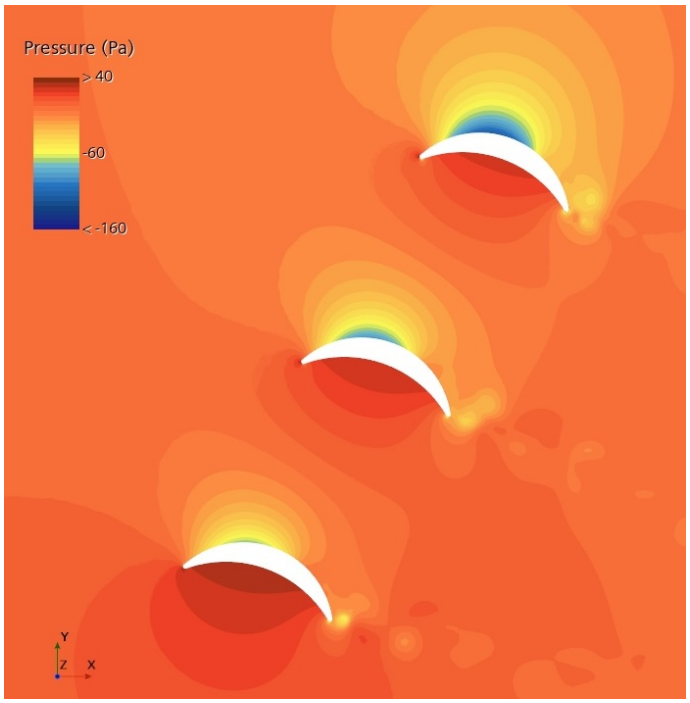

Figure 5.15: Top view of the pressure distribution of the area around each wingsail in AWA 120°.

Velocity distribution for CFD at AWA 60, 90 and 120 degrees

Here, the velocity distribution is presented for the different apparent wind angles with a top view of the wingsails arrangement. The color bar represents high velocity in red reaching values around 16.9 m/s, and low velocity in blue going down to 0 m/s.

Figures 5.16, 5.17 and 5.18 show the velocity distribution around the wingsails for 60, 90, and 120 degrees. Following Bernoulli's principle, see Equation 5.1, high velocity equals low pressure and vice versa. At AWA 60 degrees (Figure 5.16), the front wingsail shows high velocity on the suction side and it can be seen that the interaction from the pressure side of the front sail to the middle and back sails slows the velocity of the flow, influencing the velocity distribution along the other two wingsails. This is not the case for AWA 90 and 120 degrees, and looking at the drag coefficients, it is an indication that this affects the drag since the drag for the middle sail at AWA 60 degrees is the only one that is higher than the lift. At all AWA's, the area around the wingsails obey the Bernoulli's principle where on the suction side the pressure was low before, the velocity is high, and on the pressure side where the pressure was high, the velocity is low. Also, for all cases it is visible that the velocity reaches 0 m/s at the trailing edge. That is called the stagnation point and to satisfy the Kutta condition for sharp-edged bodies, it is important that the stagnation point is located exactly at the trailing edge. This means that there is a circulation at this area which is crucial for lift.

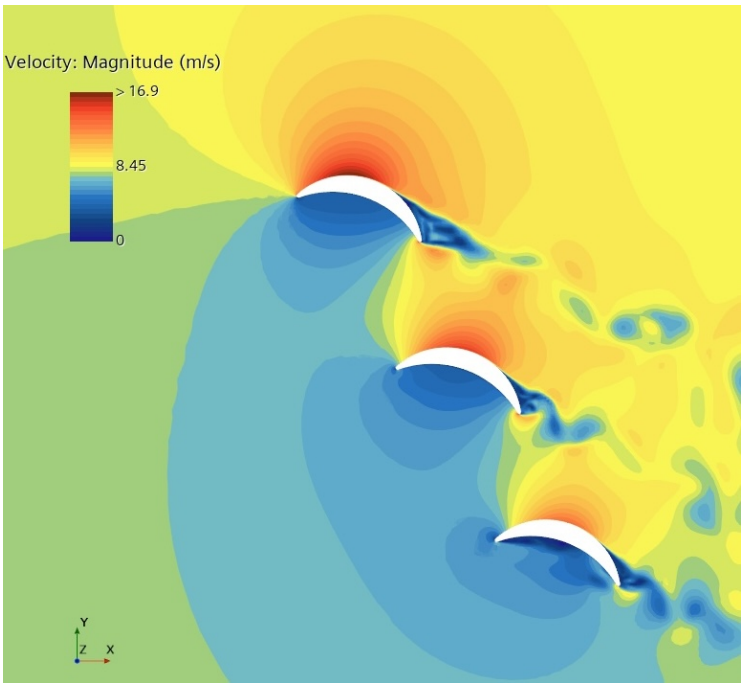

Figure 5.16: Top view of the sails showing the velocity distribution around each sail in AWA 60°.

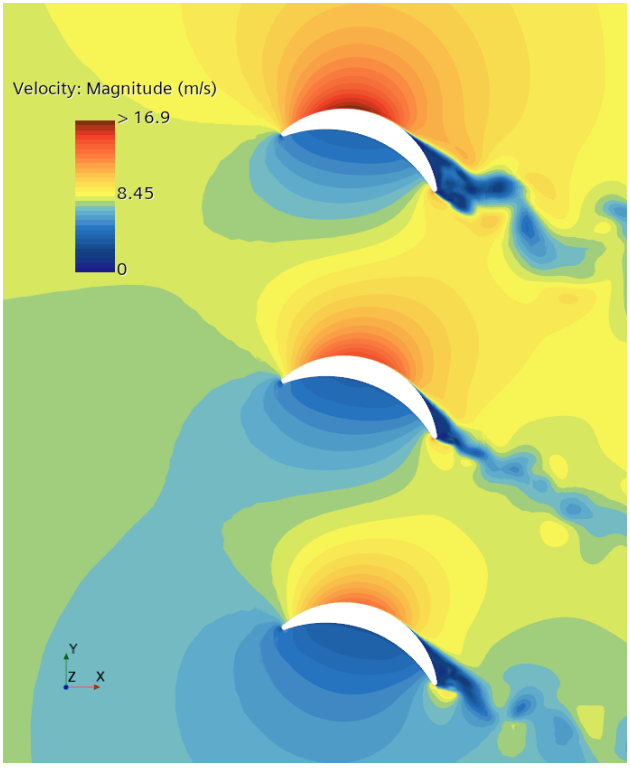

Figure 5.17: Top view of the velocity distribution of the area around each wingsail in AWA 90°.

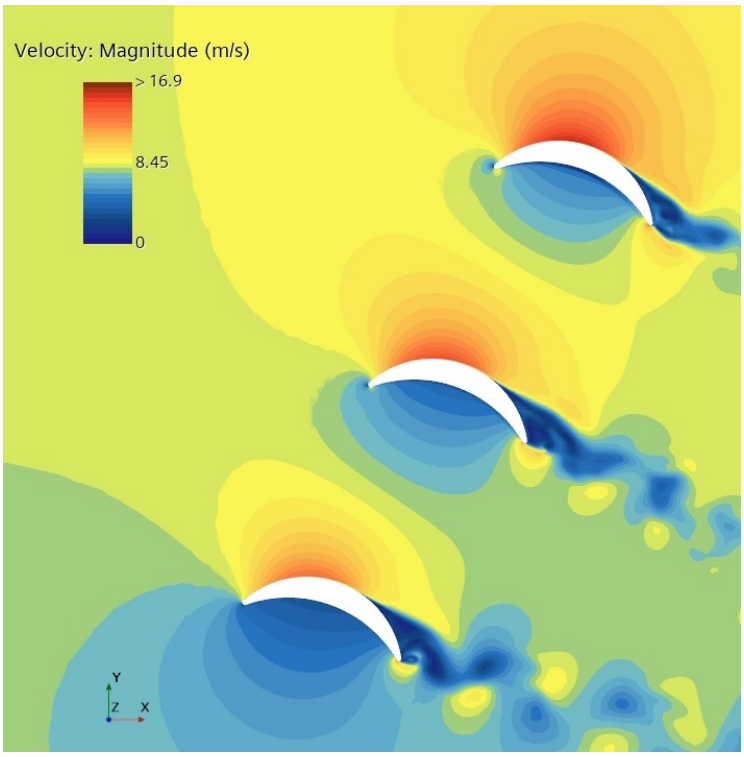

Figure 5.18: Top view of the velocity distribution of the area around each wingsail in AWA 120°.

Equation 5.1, shows the Bernoulli's principle. Due to Bernoulli's principle, the pressure at the lower surface shall be higher than it at the upper boundary, which leads to the lift. It also shows that the velocity magnitude and the pressure magnitudes are the opposite.

$$\frac{v^2}{2} + gz + \frac{p}{\rho} = constant \tag{5.1}$$

Turbulent kinetic energy for CFD at AWA 60, 90 and 120 degrees

The turbulent kinetic energy describes the transition from laminar flow to turbulent flow. This transition is influenced by the Reynolds number. The color scale indicates the intensity of the turbulent kinetic energy in the unit J/kg. The scale starts from 0.000167 J/kg and is represented in gray, and for the maximum value which is around 2.01 J/kg, the dark blue color is used. Where the area on the suction side starts turning blue (from the leading edge to the trailing edge), that is a visualization of the laminar-turbulent transition. If the transition area is located near the leading edge, like in all of the cases presented in Figures 5.19, 5.20 and 5.21, it means that the boundary layer is turbulent along the entire suction side. Despite all sails in all AWA cases having the entire suction side turbulent, the strength of the turbulent kinetic energy varies between sails. The highest values occur at the front sail for all apparent wind angles and is the lowest at the back sail, however the energy strength is the most similar at the 120 degrees AWA.

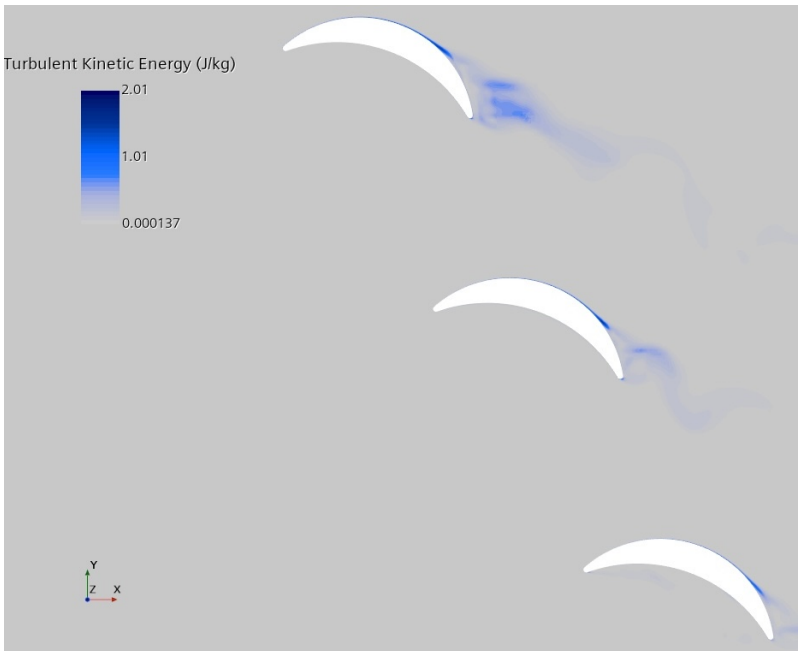

Figure 5.19: Top view of the wingsails showing the turbulent kinetic energy where the flow transitions from laminar to turbulent (AWA 60°).

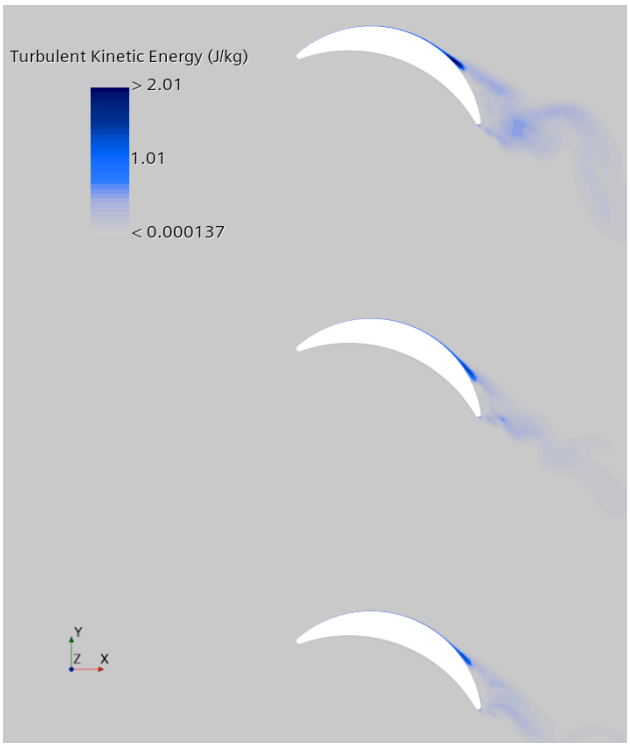

Figure 5.20: Top view of the wingsails showing the turbulent kinetic energy where the flow transitions from laminar to turbulent (AWA 90°).

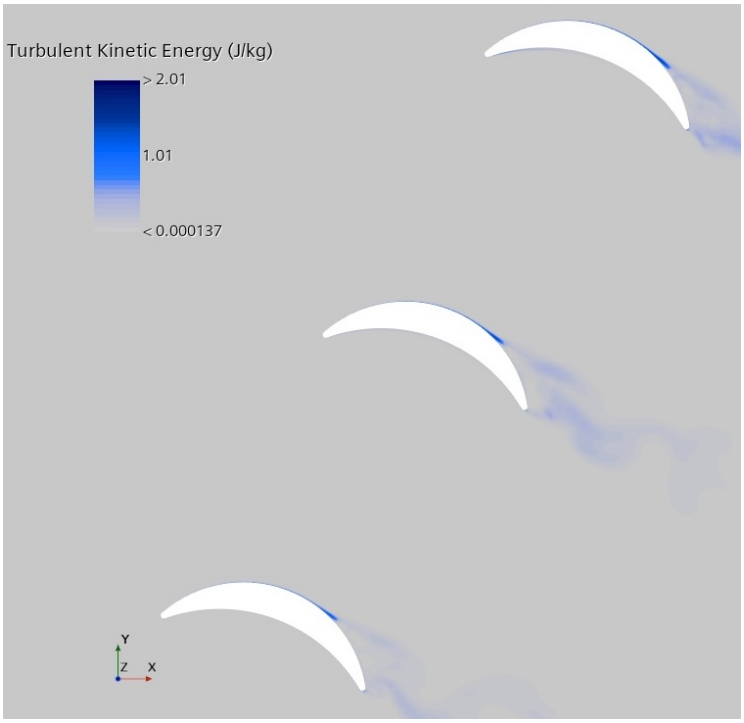

Figure 5.21: Top view of the wingsails showing the turbulent kinetic energy where the flow transitions from laminar to turbulent (AWA 120°).

5.2 FSI results for AWA 90 degrees

The FSI results for 90-deg AWA is presented in this Section. The results discussed and analyzed for the FSI simutaion are the lift, drag, and moment coefficients, tip displacement, maximum von Mises stress, pressure distribution, velocity distribution, and the turbulent kinetic energy. In all the plots, like for the CFD results, the back sail is represented in red, the middle sail is blue, and the back sail is green. The data used is from 5 seconds to 16 seconds, for all the plots and the velocity and pressure distribution are examined at 16 seconds. This is because FSI coupling usually requires a few seconds to eliminate the initial non-steady-state start-up effect.

Lift coefficient

Figure 5.22 presents the plot for the lift coefficients of each sail. The front sail has the highest lift coefficient and the back sail has the lowest.

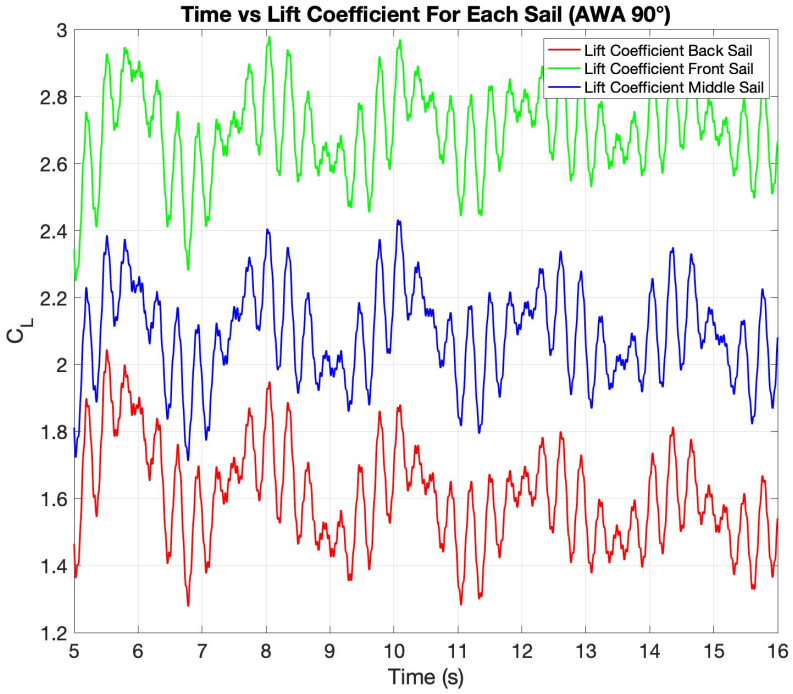

Figure 5.22: Plot showing the FSI lift coefficient for each sail in apparent wind angle 90°.

Drag coefficient

Figure 5.23 shows the plot for the drag coefficients for each sail. There is a high oscillation in this plot, therefore it's difficult to see the exact values. However, the top values are for the front sail and the lowest for the back sail. Later in this chapter, the time-averaged values are presented where it's calculated the average value for each sail to see the difference between them.

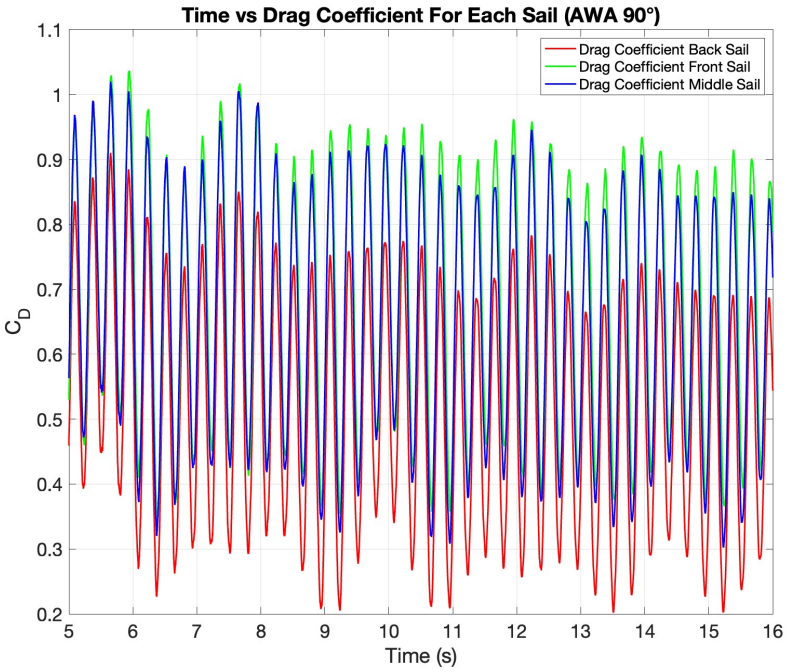

Figure 5.23: Plot showing the FSI drag coefficient for each sail in apparent wind angle 90°.

Moment coefficient

Moment coefficient plot can be seen in Figure 5.24. Here the values are the opposite to the lift and drag where now the back sail has the highest value and front sail has the lowest value (a negative value). The middle sail oscillates around 0, so it's necessary to take the average of this value in this timeline to see wheather or not the average value is negative or positive.

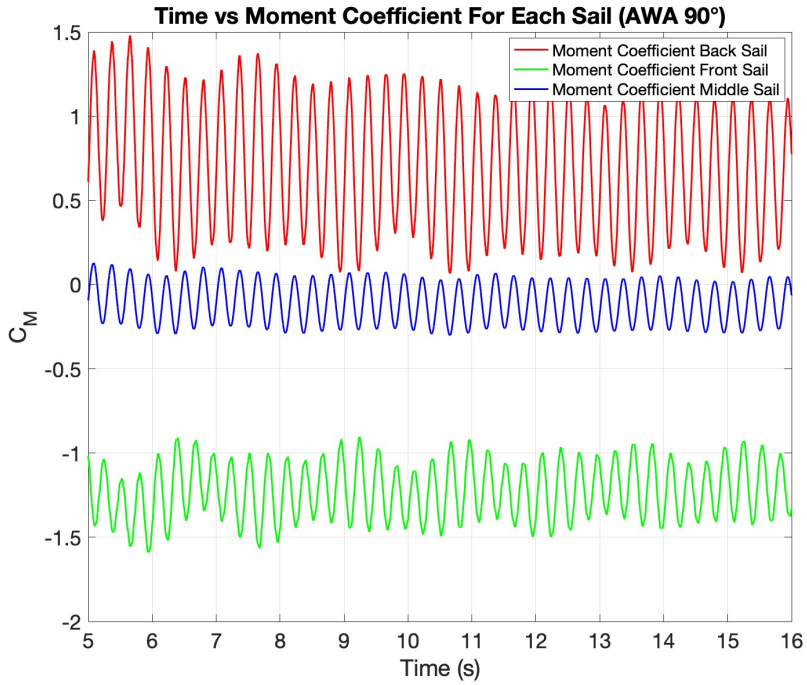

Figure 5.24: Plot showing the FSI moment coefficient for each sail in apparent wind angle 90°.

Time averaged values (FSI)

Time average values of the force coefficients between 5 seconds and 16 seconds is shown in Table 5.3. Figure 5.25 shows the lift coefficient each sail. As can be observed from the picture, the front sail has the highest lift coefficient, the back sail has the lowest lift coefficient, and the middle sail is between those two plots. This is because the front wingsail experiences the airflow without any influence from other wingsails, producing maximum lift. However, the middle sail and the back sail show progressively lower lift coefficients. This is due to the wake and downwash from the front sail, where the airflow is pushed downwards behind each sail consequently reducing lift. The back sail experiences the lowest lift coefficient due to its significant shadowing effects, which is the reduced effective wind area for downstream wingsails, leading to reduced performance.

Table 5.3: Time-averaged force coefficients for AWA 90° for each sail between 5s and 16s.

AWA	Sail	C_L	C_D	C_M
90°	Sail F	2.699	0.676	-1.224
	Sail M	2.091	0.649	-0.106
	Sail B	1.607	0.517	0.706

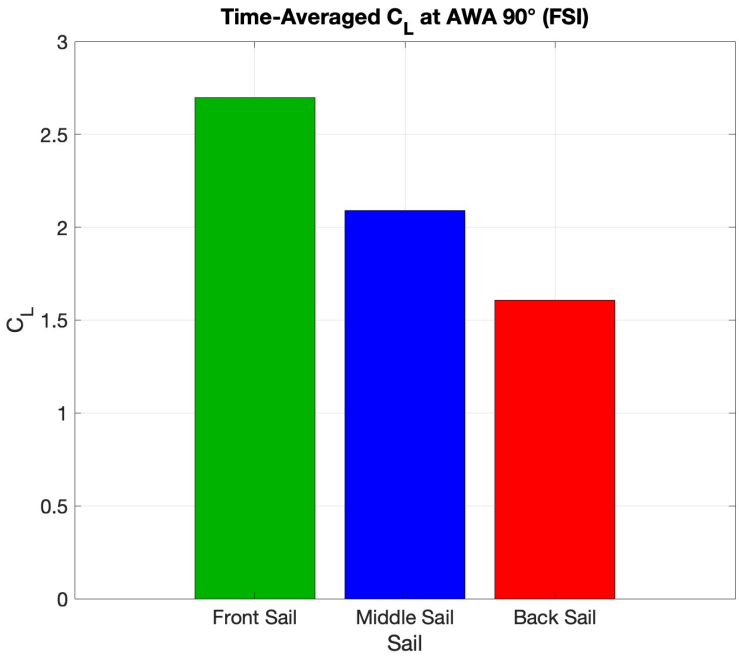

Figure 5.25: Time-averaged values for the lift coefficient for FSI simulation at AWA 90°.

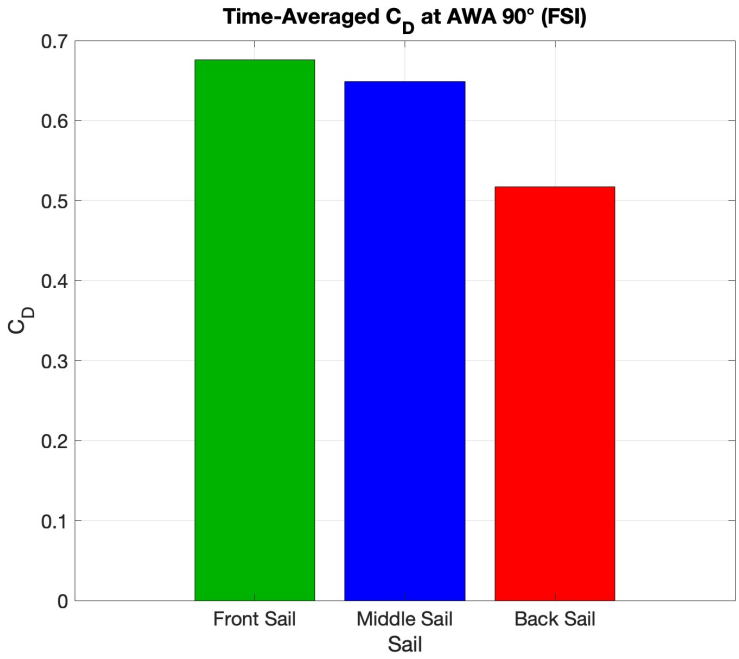

Figure 5.26: Time-averaged values for the drag coefficient for FSI simulation at AWA 90°.

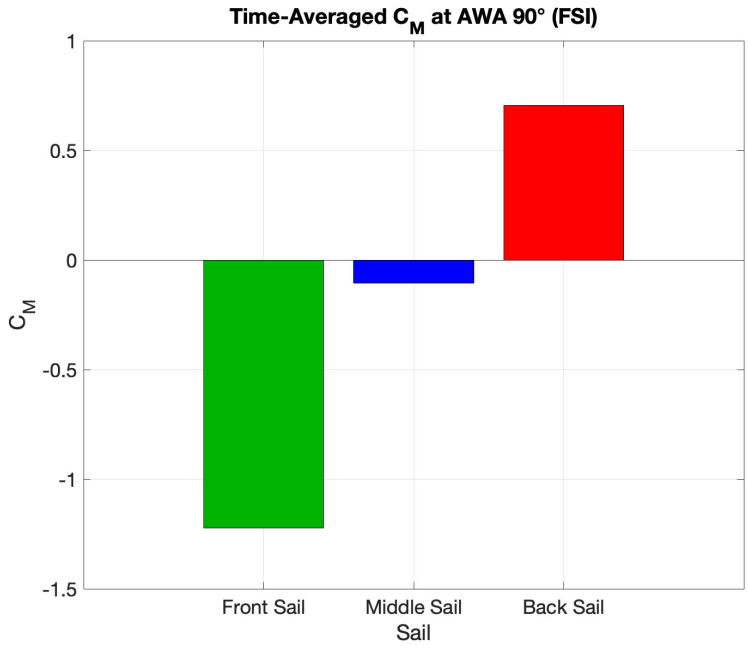

Figure 5.27: Time-averaged values for the moment coefficient for FSI simulation at AWA 90°.

The lift coefficient data can be seen in Figure 5.25 where the front sail has the highest life and back sail has the lowest lift. For the drag it's the same, the front sail has the highest C_D value, while the back sail has the lowest. The front sail is exposed to undisturbed airflow as it is the first to interact with the wind. Figure 5.27 shows the time-averaged values for the moment coefficients for each sail. The front and middle sails experience negative moment because the suction is located closer to the leading edge, which generates a negative moment. In contrast, the back sail has the suction located closer to the center of the wingsail and the trailing edge, generating a positive moment.

Tip displacement

Tip displacement plot for AWA 90° can be seen in Figure 5.28. This plot describes the tip displacement in y-direction for each wingsail. The front wingsail experiences the highest tip displacement due to its greater aerodynamic force. The middle sail shows moderate displacement, slightly less than that the front wingsail. The back sail has the lowest displacement, which is attributed to its lower lift and drag coefficients, as well as its pressure differentials. A 3 dimensional representation of the tip displacement can be seen in Figure 5.29, where the highest displacement can be seen in the color red. It's visible that the front sail experiences more tip displacement than the other two sails, making it more prone to damage.

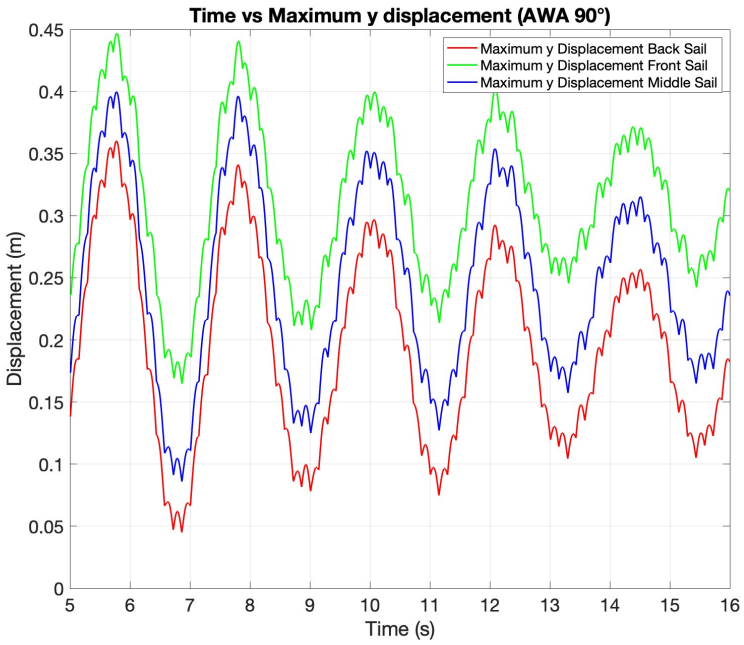

Figure 5.28: Plot showing the tip displacement, maximum displacement in y direction, for each sail in apparent wind angle 90°.

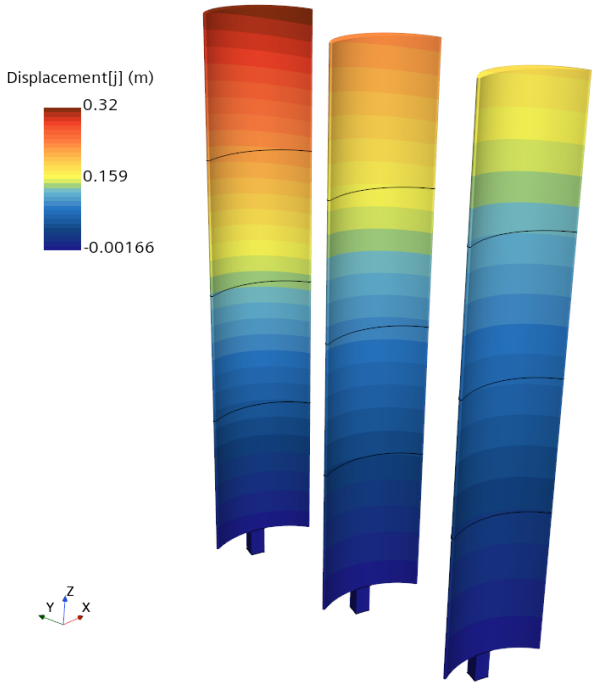

Figure 5.29: This image shows the 3D representation of the maximum tip displacement (displacement in y-direction) that each sail experiences in AWA 90°.

Maximum von Mises stress

Maximum von Mises stress for AWA 90° can be seen Figure 5.30. The time-averaged values for the front sail are 3.83 MPa, the middle sail is 3.49 MPa and for the back sail it's 2.60 MPa. The front sail has the highest von Mises stress, which means that it experiences the highest combined mechanical loading. That concurs with the other data, such as maximum tip displacement as well as the highest lift. This is a direct result of the front sail having the highest lift and therefore the highest pressure difference between the suction and pressure side.

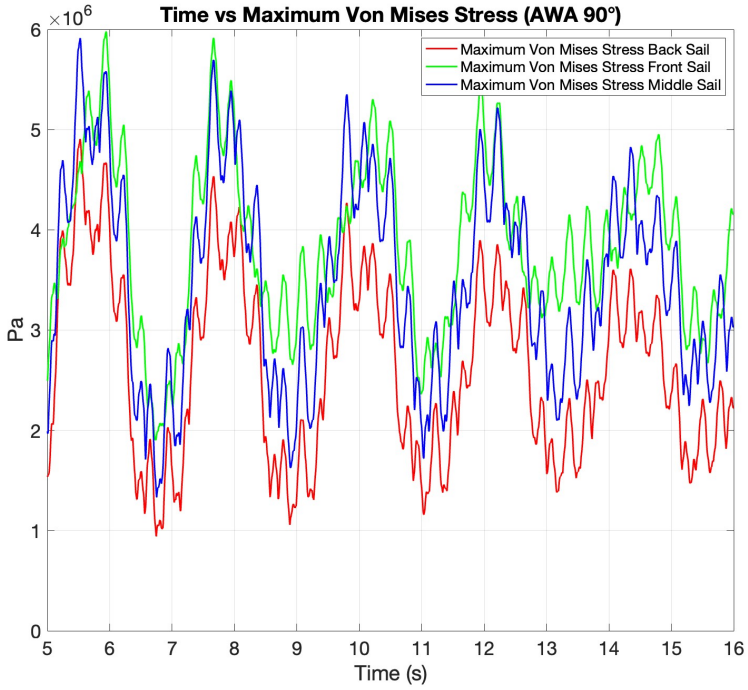

Figure 5.30: Plot showing the maximum von Mises stress for each sail in apparent wind angle 90°.

Pressure distribution

FSI pressure distribution is presented in Figure 5.31. For all sails, it can be seen that the pressure on the suction surface is a lot lower while the pressure on the pressure surface is higher. This pressure difference, like has been mentioned before, generates lift. The highest difference between pressure and suction side is for the front sail, therefore the front sail has the highest lift and opposite for the back sail which has lower pressure difference and therefore lower lift. The placement of the suction is closer to the leading edge for the front and middle sail, generating a negative lift and for the back sail it's located more to the center of the sail, resulting in positive lift, see Figure 5.24.

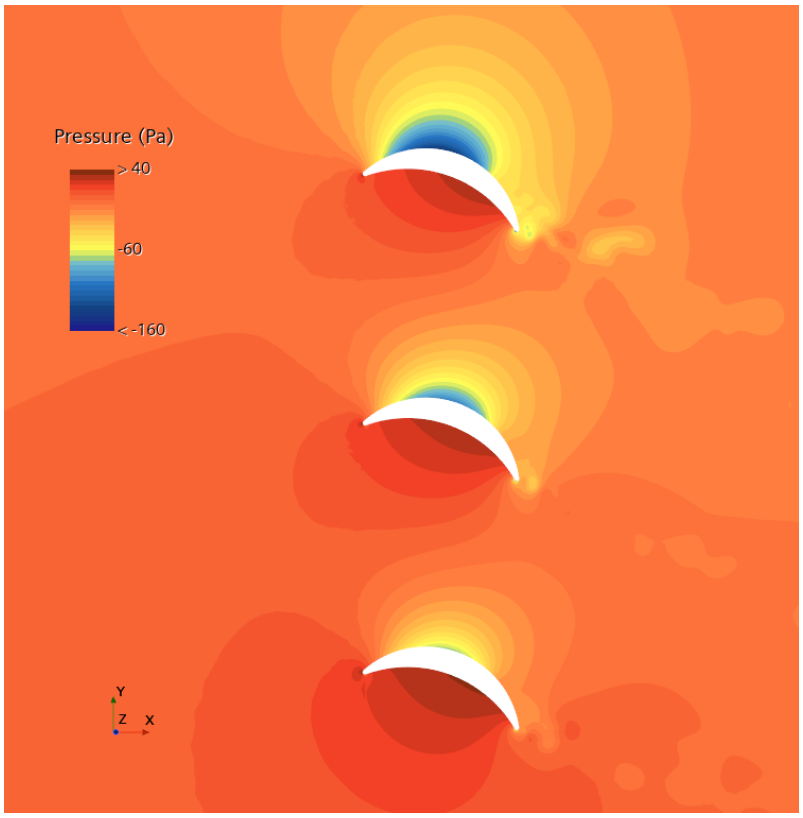

Figure 5.31: Top view of the sails showing the pressure distribution around each sail in AWA 90°.

Velocity distribution - FSI AWA 90°

Figure 5.32 shows the plane section of the velocity distribution around each wingsail. High velocity on the suction surface and low velocity on the pressure surface, according to Bernoulli's principle. The front wingsail experiences a higher velocity than the other wingsails and the stagnation point for each sail is located at the trailing edge, satisfying the Kutta condition.

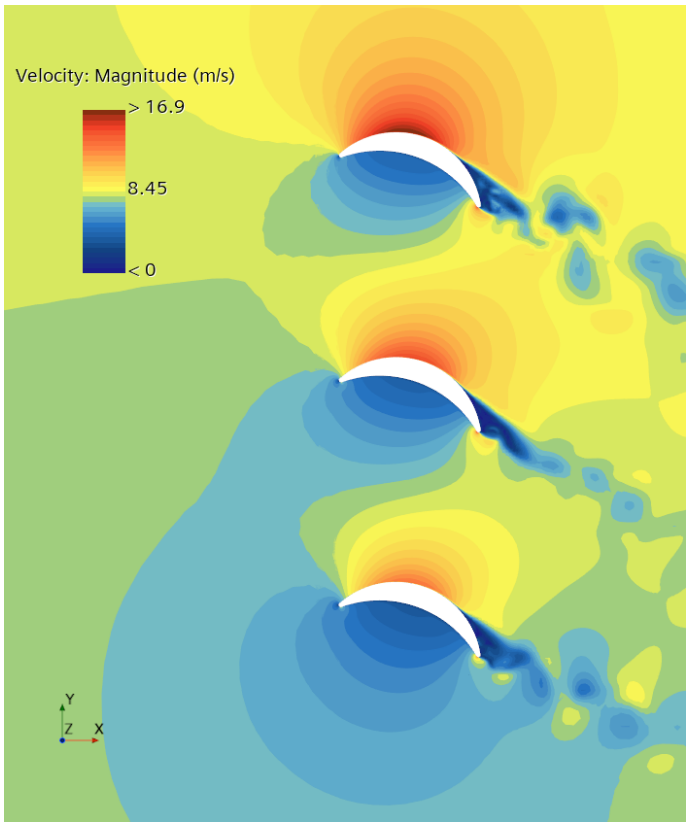

Figure 5.32: Top view of the sails showing the velocity distribution around each sail in AWA 90°.

Turbulent kinetic energy

The turbulent kinetic energy is presented in Figure 5.33, and shows the point where flow transitions from laminar to turbulent. The transition area is at a similar place for all sails, close to the leading edge, indicating a turbulent boundary layer on the entire suction side. However, the front wingsail has higher values of turbulent kinetic energy than the other two.

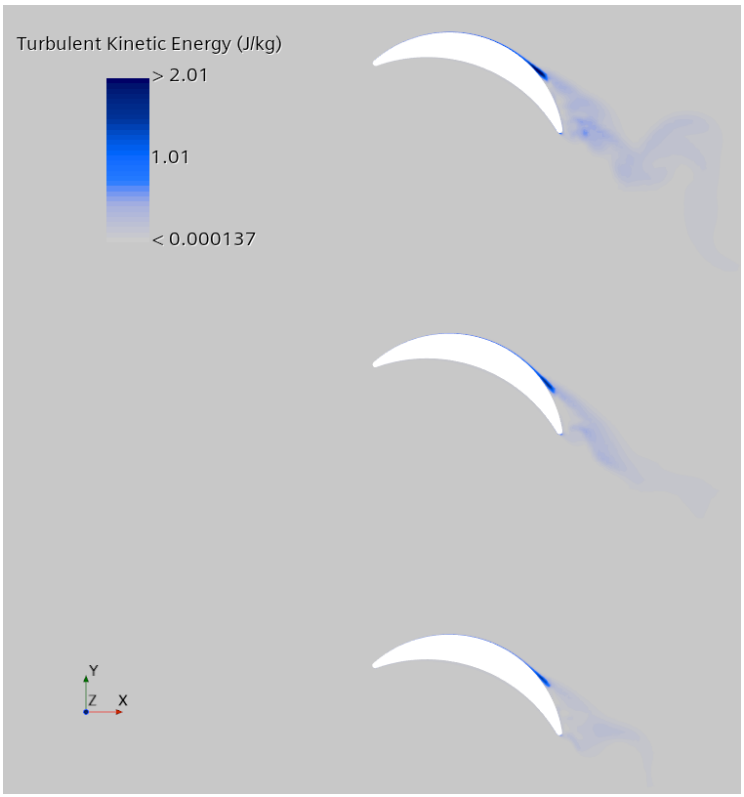

Figure 5.33: Top view of the wingsails showing the turbulent kinetic energy where the flow transitions from laminar to turbulent (AWA 90°).

6
Conclusion

This thesis investigates the aerodynamic and fluid-structure interaction (FSI) effects of multiple crescent-shaped wingsails. By using two-way coupled FSI simulation techniques, the relationship between aerodynamic forces and structural responses is examined for a three wingsail system. The objectives are to apply FSI to analyze aerodynamic interactions, model the physical interplay between adjacent sails, and quantify their impact on both propulsion efficiency and structural performance.

The simulation results indicated that the front sail consistently experienced the highest aerodynamic loads, including lift, drag, and moment. This underscores its crucial role in propulsion while also revealing structural vulnerabilities. Among the apparent wind angles studied, 60° provided the best aerodynamic performance, marking it as the optimal condition for the wingsail arrangement.

This thesis presented an analysis of the aerodynamic and structural behavior of the three wingsails in different apparent wind angles using CFD and FSI simulations. The conclusion is presented below.

- **Reinforcement of the front sail:**
  From the FSI results, it can be determined where the structure will experience the most displacement, as demonstrated in Figure 5.29. Therefore, this sail must be designed to be strong enough to support this displacement without fracturing.
- **Optimal AWA from CFD simulations:**
  From the CFD results, it can be concluded that the AWA with greater propulsion efficiency is the 60 degrees, under the condition where all wingsails share the same AOA. And the AWA with less performance is 120 degrees.
- **Force coefficients for FSI:**
  For FSI simulation with AWA 90 degrees, the front sail experiences higher lift, drag and moment coefficients than the middle and back sail. This is due to the influence from the front sail to the other sails. The front sail is exposed to undisturbed flow. This conclusion confirms Zhu (2024) findings.
- **Justification for FSI simulation:**
  After performing both FSI and CFD simulations, it can be concluded that the CFD simulation is not enough to validate the interaction between the sails. CFD only simulates the fluid (air) but not for the structure itself and therefore from CFD simulations it's not possible to see tip displacements or the stress distributions, which are crucial for determining whether or not the sails can

handle certain situations out on the open sea.

- **Save computational time and cost:**
  Only use a finer mesh in the flow direction. In Figure 6.1, the flow direction is represented diagonally from the wingsail to the bottom of the figure.

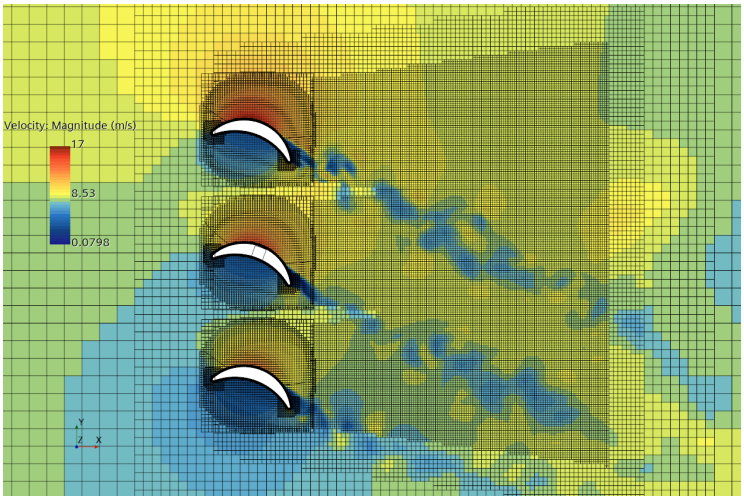

Figure 6.1: Top view of the sails showing the mesh for the wake refinement and the flow direction.

6.1 Future prespective

- **Hull interaction:**
  Investigate the interaction between the wingsails and the ship's hull. The proximity and geometry of the hull can influence flow characteristics and aerodynamic performance
- **Detailed structure:**
  More detailed structure of the wingsails to obtain a more accurate prediction of the stress distribution, deformation, and structural behavior under different load cases.
- **Additional AWA's for the FSI simulation:**
  Fluid-structure interaction simulations should be conducted for apparent wind angles of 60° and 120°. And analyze lift, drag, and moment coefficients, tip displacement, maximum von Mises stress, pressure distribution, velocity distribution, and the turbulent kinetic energy. Compare the simulation results with CFD results for AWA 60° and 120°.
- **Computational efficiency improvements:**
  Future research could also explore mesh refinement strategies in areas of critical flow to reduce simulation costs while maintaining accuracy.

Bibliography

Anderson, J. D. (2023a). Introduction to boundary layers [Accessed: 2025-05-11].

Anderson, J. D. (2023b). Thin airfoil theory [Accessed: 2025-05-11].

ANSYS. (2025). Laminar vs. turbulent flow: What's the difference? [Accessed: 2025-05-12]. https://www.ansys.com/blog/laminar-vs-turbulent-flow

Atoyebi, E. O., & Ojo-Kupoluyi, O. J. (2024). *Comprehensive materials processing (second edition)*. Elsevier. https://www.sciencedirect.com/referencework/9780323960212/comprehensive-materials-processing

Berger, E., & Wille, R. (1972). Periodic flow phenomena [Accessed: 2025-05-24]. *Annual Review of Fluid Mechanics*, *4*, 313–340. https://doi.org/10.1146/annurev.fl.04.010172.001525

Bisbee, J., Halloran, P., & Larkin, N. (1995). *Sailing and the tech dinghy: Instruction manual* [Revised edition]. Massachusetts Institute of Technology. Cambridge, Massachusetts. https://sailing.mit.edu/lts/sailing-booklet/booklet.pdf

bound4blue. (2025). How it works — bound4blue [youtube video] [Accessed: 2025-05-13].

Burden, A., Lloyd, T., Mockler, S., Mortola, L., Shin, I. B., & Smith, B. (2010). *Concept design of a fast sail-assisted feeder container ship* (Student Research Project) (Accessed: 2025-05-13). University of Southampton.

Cabeza, L. F. (Ed.). (2022). *Encyclopedia of energy storage* [Accessed: 2025-05-22]. Elsevier. https://www.elsevier.com/books/encyclopedia-of-energy-storage/cabeza/978-0-12-819730-1

Chen, Y., Mu, X., Wang, T., Ren, W., Yang, Y., Wang, Z. L., Sun, C., & Gu, A. Y. (2016). Flutter phenomenon in flow driven energy harvester–a unified theoretical model for "stiff" and "flexible" materials [Accessed: 2025-05-24]. *Scientific Reports*, *6*, 35180. https://doi.org/10.1038/srep35180

Clancy, L. J. (1975). *Aerodynamics*. Pitman Publishing.

Eisenbach, S., & Friedrich, R. (2008). Large-eddy simulation of flow separation on an airfoil at a high angle of attack and re $= 10^5$ using cartesian grids. *Theoretical and Computational Fluid Dynamics*, *22*(3), 213–225. https://doi.org/10.1007/s00162-007-0072-z

European Commission. (2025). Reducing emissions in the shipping sector [Accessed: 2025-05-13].

Guzelbulut, C., Badalotti, T., & Suzuki, K. (2024). Optimization techniques for the design of crescent-shaped hard sails for wind-assisted ship propulsion [Accessed: 2025-05-11]. *Ocean Engineering*, *312*, 119142. https://doi.org/10.1016/j.oceaneng.2024.119142

Hebert, C., Cowan, D., Attar, P. J., & Weiseman, C. D. (2025). *Aerodynamic flutter* [Contributed by NextGen Aeronautics and NASA Langley Research Center. Accessed: 2025-05-24]. https://www.nasa.gov/sites/default/files/atoms/files/aerodynamic_flutter.pdf

Hua, Y., Zeng, X., & Li, S. (2012). Research on the aerodynamic characteristics of ellipse wing sail [Accessed: 2025-05-13]. *Advanced Materials Research*, *347–353*, 2249–2254. https://doi.org/10.4028/www.scientific.net/AMR.347-353.2249

IMO. (2020). Fourth imo greenhouse gas study 2020 [Accessed: 2025-05-13].

IMO. (2023a). 2023 imo strategy on reduction of ghg emissions from ships [Accessed: 2025-05-13].

IMO. (2023b). Imo approves net-zero regulations [Accessed: 2025-05-13].

Jr., J. D. A. (2015). *Introduction to flight* (8th ed.) [Accessed: 2025-05-11]. McGraw-Hill Education. https://aerospace.gdgoenka-university.com/wp-content/uploads/2023/10/introduction-to-flight-8th

Kimball, J. (2010). *Physics of sailing*. CRC Press, Taylor & Francis Group.

Kuethe, A. M., & Chow, C.-Y. (1997, December). *Foundations of aerodynamics: Bases of aerodynamic design* (5th ed.). John Wiley & Sons.

Laboratory of Fluid Mechanics and Instabilities (LFMI). (2025). *Vortex-induced vibrations (viv) of porous objects* [Accessed: 2025-05-24]. https://www.epfl.ch/labs/lfmi/projects/viv-porous-objects/

Leishman, J. G. (2025). Thin airfoil theory [Accessed: 2025-05-11]. In *Introduction to aerospace flight vehicles*. Embry-Riddle Aeronautical University. https://eaglepubs.erau.edu/introductiontoaerospaceflightvehicles/chapter/thin-airfoil-theory/

Liu, T., Wang, S., Liu, H., & He, G. (2023). Engineering perspective on bird flight: Scaling, geometry, kinematics and aerodynamics [Accessed: 2025-05-11]. *Progress in Aerospace Sciences*, *152*, 100994. https://doi.org/10.1016/j.paerosci.2023.100994

Liu, Y., Zhang, H., & Ahmed, A. (2023). Fluid–structure interaction analysis of aeroelastic behavior in thin wings using coupled numerical methods. *Arabian Journal for Science and Engineering*, *49*. https://doi.org/10.1007/s13369-023-08314-6

Lu, R., & Ringsberg, J. W. (2020). Ship energy performance study of three wind-assisted ship propulsion technologies including a parametric study of the flettner rotor technology [Accessed: 2025-05-13]. *Ships and Offshore Structures*, *15*(3), 249–258. https://doi.org/10.1080/17445302.2019.1612544

Nakamura, T., Kaneko, S., Inada, F., et al. (2013). *Flow-induced vibrations: Classifications and lessons from practical experiences* [Accessed: 2025-05-24]. Butterworth-Heinemann.

Nikmanesh, M. (2021, July). *Sailing performance analysis using cfd simulations: A study on crescent shaped wing profiles* (Publication No. 2021:79) [Master's thesis in Naval Architecture and Ocean Engineering]. Chalmers University of Technology [Accessed: 2025-05-11].

Oceanbird. (2025). Wind assist – oceanbird wing 560 [Accessed: 2025-05-13].

Ouchi, K., Uzawa, K., & Kanai, A. (2011). Huge hard wing sails for the propulsor of next generation sailing vessel [Accessed: 2025-05-13]. *Proceedings of the Second International Symposium on Marine Propulsors (smp'11)*, 1–5. https://www.marinepropulsors.com/proceedings/2011/FA1-3_Ouchi.pdf

Ouchi, K., Uzawa, K., Kanai, A., & Katori, M. (2013). "wind challenger" the next generation hybrid sailing vessel [Accessed: 2025-05-13]. *Proceedings of the Third International Symposium on Marine Propulsors (smp'13)*, 562–567. https://www.marinepropulsors.com/proceedings/2013/11B.3.pdf

Schlichting, H., & Gersten, K. (2017). *Boundary-layer theory* (9th ed.) [With contributions by Egon Krause and Herbert Oertel Jr.; translated by Katherine Mayes]. Springer-Verlag Berlin Heidelberg. https://doi.org/10.1007/978-3-662-52919-5

Singh, M. K., & Mittal, S. (2023). Vortex-induced vibration of a circular cylinder in the subcritical reynolds number regime: Effect of reduced velocity and mass ratio [Accessed: 2025-05-24]. *Theoretical and Computational Fluid Dynamics*. https://doi.org/10.1007/s00162-023-00644-3

Stack Exchange. (2017). What is the physical meaning of circulation found in kutta condition? [Accessed: 2025-05-11]. https://aviation.stackexchange.com/questions/47251/what-is-the-physical-meaning-of-circulation-found-in-kutta-condition

The Aviation History Online Museum. (2002). Laminar flow airfoil [Accessed: 2025-05-12]. http://www.aviation-history.com/theory/lam-flow.htm

Thies, F., & Fakiolas, K. (2022). Wind propulsion [Accessed: 2025-05-13]. In *Sustainable energy systems on ships* (pp. 353–401). Elsevier. https://doi.org/10.1016/B978-0-12-824471-5.00016-5

United Nations. (2025). Energy — united nations sustainable development [Accessed: 2025-05-13].

United Nations Conference on Trade and Development. (2024). Review of maritime transport 2024: Navigating maritime chokepoints (overview) [Accessed: 2025-05-13].

Wikipedia contributors. (2025). Kármán vortex street [Accessed: 2025-07-15]. https://en.wikipedia.org/wiki/K%C3%A1rm%C3%A1n_vortex_street

Wunderground. (2025). Whirls, curls, and little swirls: Science behind von kármán vortices [Accessed: 2025-07-15].

Xu, B., Wang, T., Yuan, Y., Zhao, Z., & Liu, H. (2018). A simplified free vortex wake model of wind turbines for axial steady conditions. *Applied Sciences*, *8*(5), 844. https://doi.org/10.3390/app8050844

Zhang, Y., & Wang, Z. (2022). Shedding vortex characteristics analysis of naca 0012 airfoil at low reynolds numbers. *Results in Physics*, *28*, 104681. https://doi.org/10.1016/j.rinp.2022.104681

Zhu, H. (2024). *Analysis and evaluation of wingsails with crescent-shaped profiles – from aerodynamics to aeroelasticity* (Publication No. 5598) [PhD dissertation]. Chalmers University of Technology [Accessed: 2025-05-11].

Zhu, H., Chernoray, V., Ringsberg, J. W., Ramne, B., & Yao, H.-D. (2024). Experimental and numerical studies on moderate-re aerodynamics of cambered

thick wingsails in crescent shape [Accessed: 2025-05-13]. *SSRN Electronic Journal*. https://ssrn.com/abstract=4929670

Zhu, H., Yao, H.-D., & Ringsberg, J. W. (2024). Unsteady rans and iddes studies on a telescopic crescent-shaped wingsail [Accessed: 2025-05-11]. *Ships and Offshore Structures*, *19*(1), 134–147. https://doi.org/10.1080/17445302.2023.2256601

Zhu, H., Yao, H.-D., Thies, F., Ringsberg, J. W., & Ramne, B. (2023a). Propulsive performance of a rigid wingsail with crescent-shaped profiles [Accessed: 2025-05-11]. *Ocean Engineering*, *285*, 115349. https://doi.org/10.1016/j.oceaneng.2023.115349

Zhu, H., Yao, H.-D., Thies, F., Ringsberg, J. W., & Ramne, B. (2023b). Propulsive performance of a rigid wingsail with crescent-shaped profiles [Accessed: 2025-05-13]. *Ocean Engineering*, *285*, 115349. https://doi.org/10.1016/j.oceaneng.2023.115349

A

Appendix 1

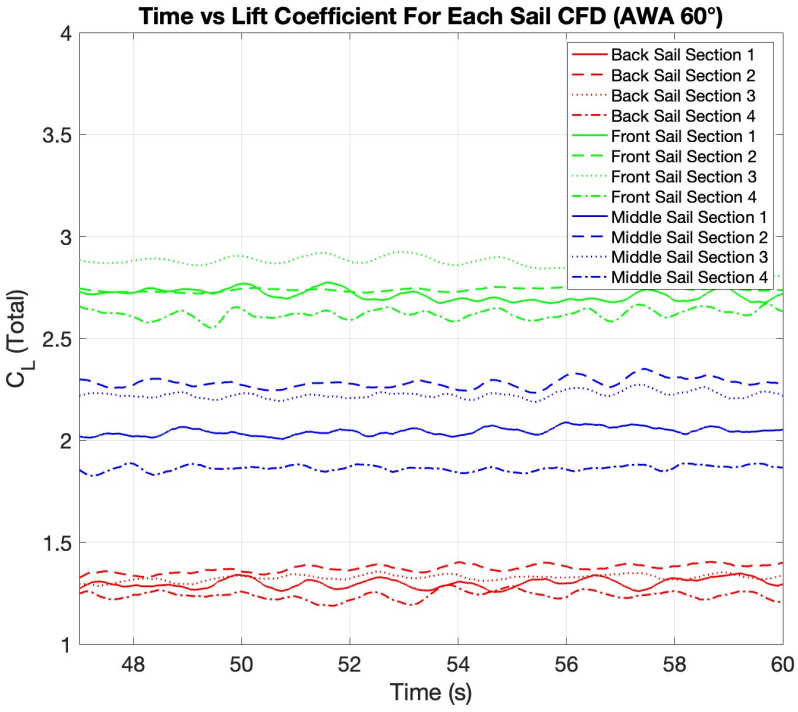

Figure A.1: Plot showing the CFD lift coefficient for each section of the sails in apparent wind angle 60°.

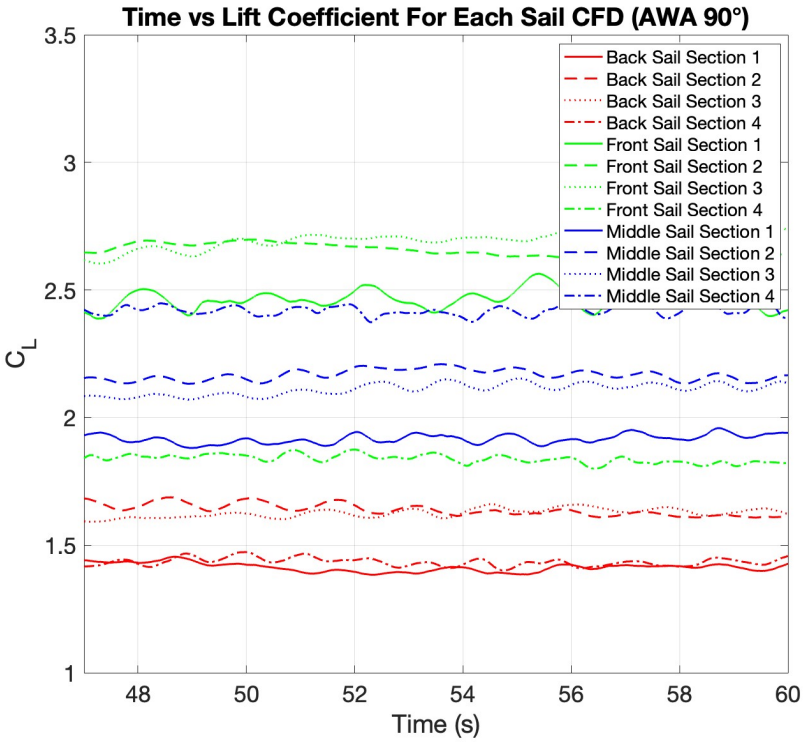

Figure A.2: Plot showing the CFD lift coefficient for each section of the sails in apparent wind angle 90°.

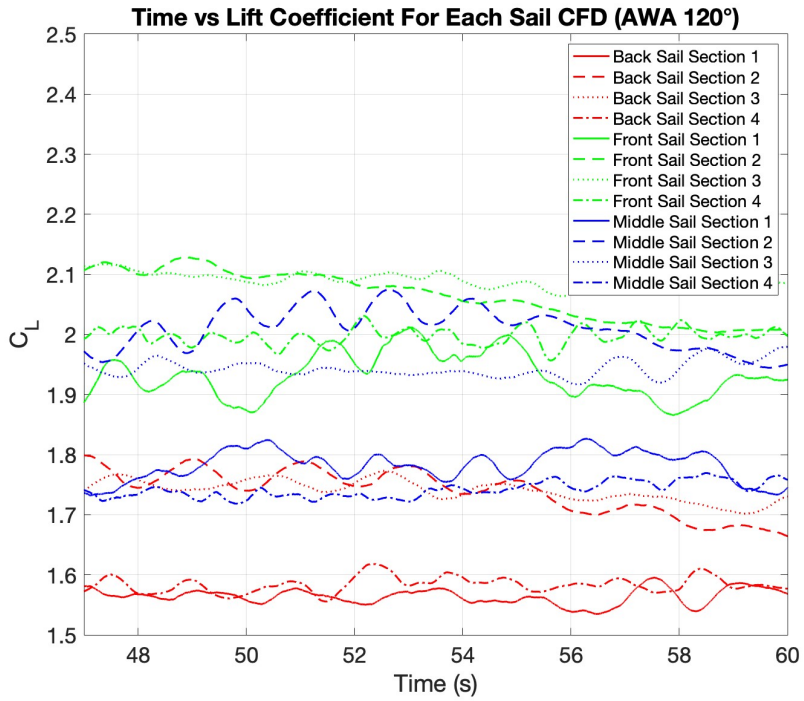

Figure A.3: Plot showing the CFD lift coefficient for each section of the sails in apparent wind angle 120°.

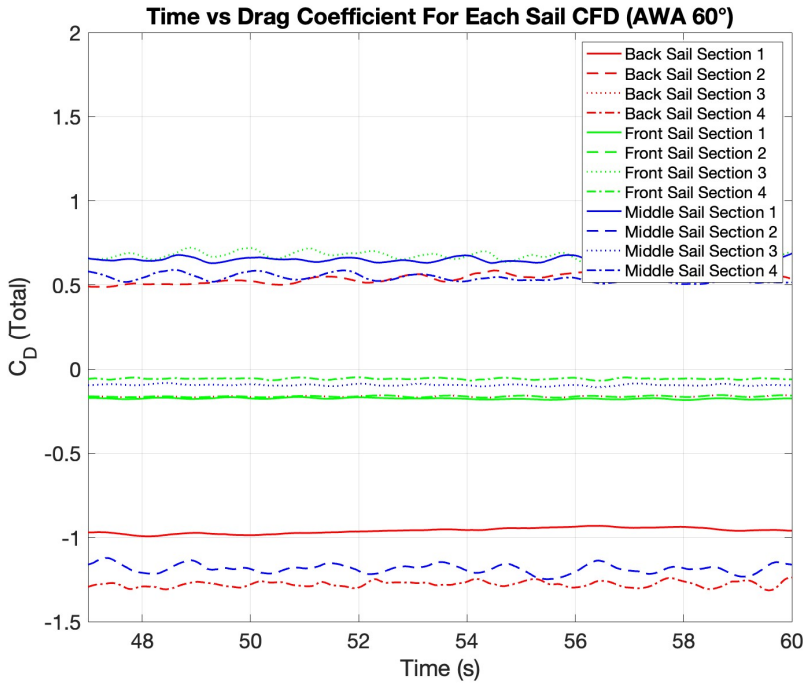

Figure A.4: Plot showing the CFD drag coefficient for each section of the sails in apparent wind angle 60°.

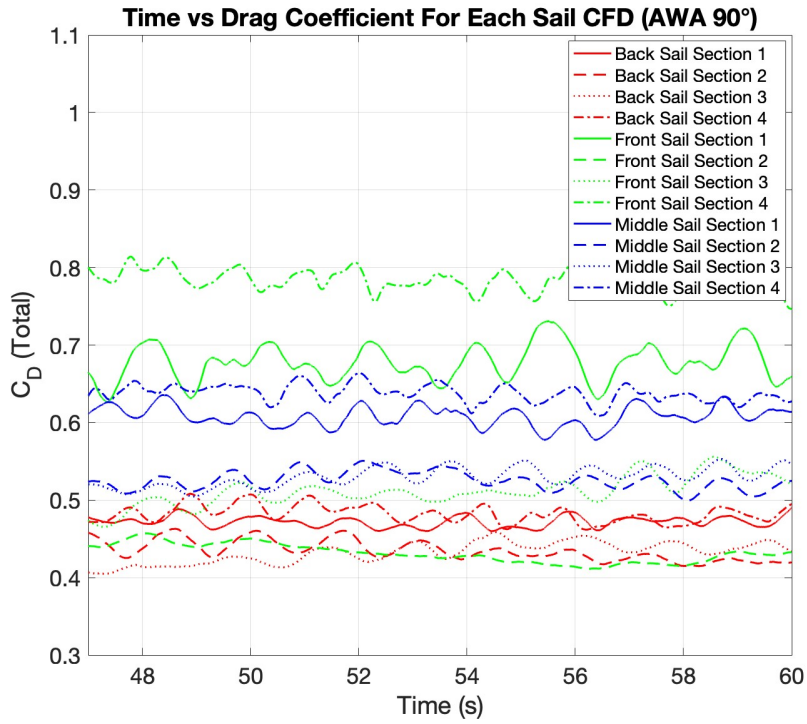

Figure A.5: Plot showing the CFD drag coefficient for each section of the sails in apparent wind angle 90°.

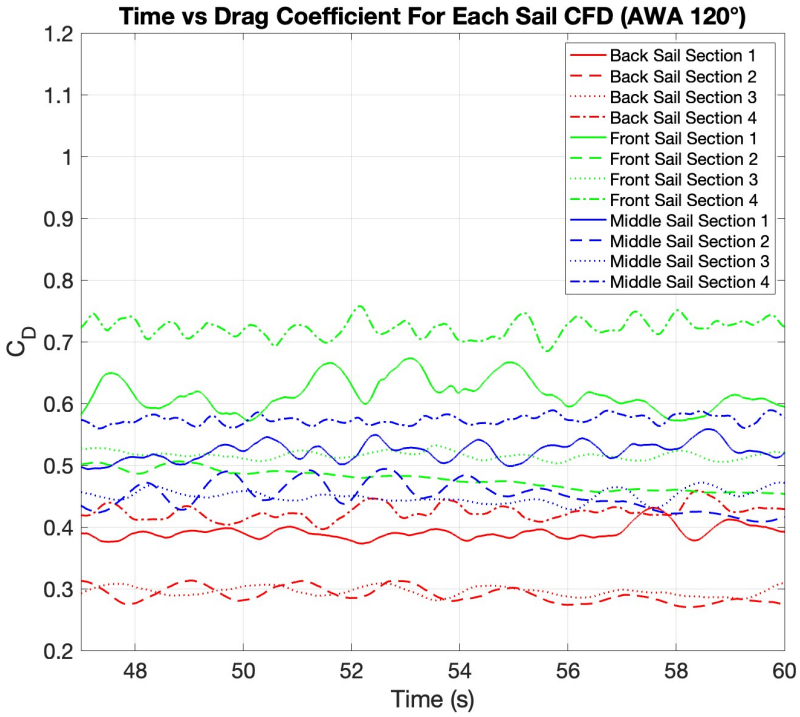

Figure A.6: Plot showing the CFD drag coefficient for each section of the sails in apparent wind angle 120°.

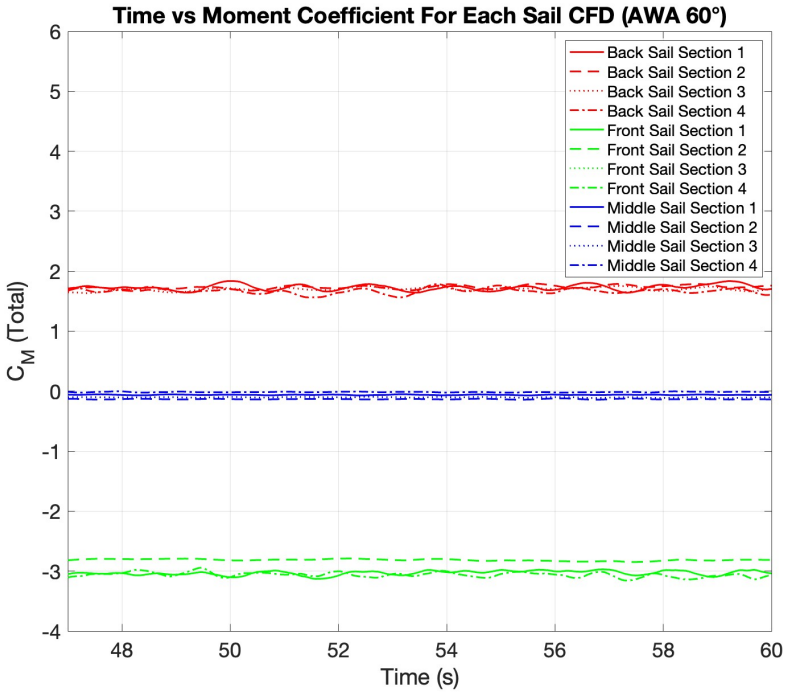

Figure A.7: Plot showing the CFD moment coefficient for each section of the sails in apparent wind angle 60°.

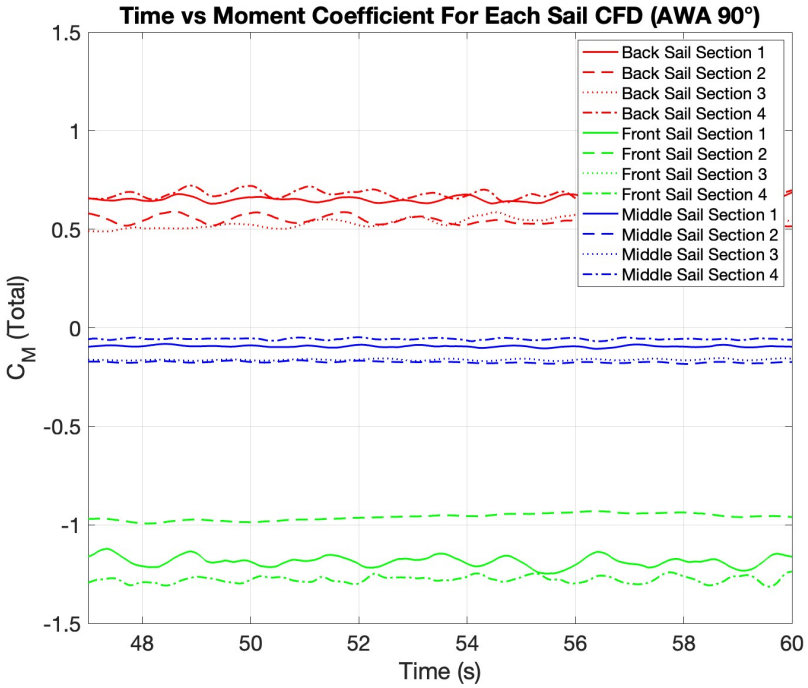

Figure A.8: Plot showing the CFD moment coefficient for each section of the sails in apparent wind angle 90°.

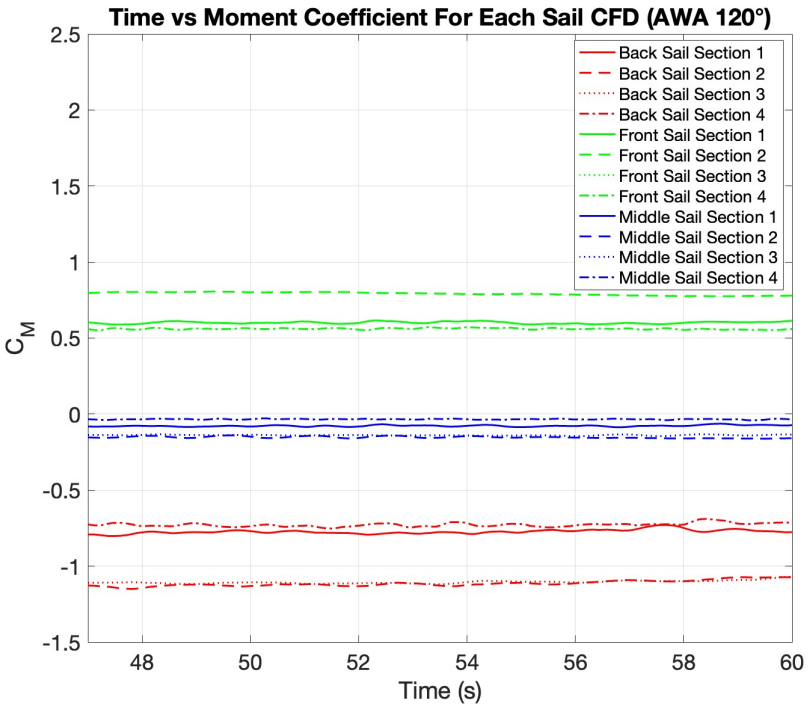

Figure A.9: Plot showing the CFD moment coefficient for each section of the sails in apparent wind angle 120°.

DEPARTMENT OF SOME SUBJECT OR TECHNOLOGY
CHALMERS UNIVERSITY OF TECHNOLOGY
Gothenburg, Sweden
www.chalmers.se

CHALMERS
UNIVERSITY OF TECHNOLOGY